



저작자표시-비영리-변경금지 2.0 대한민국

이용자는 아래의 조건을 따르는 경우에 한하여 자유롭게

- 이 저작물을 복제, 배포, 전송, 전시, 공연 및 방송할 수 있습니다.

다음과 같은 조건을 따라야 합니다:



저작자표시. 귀하는 원저작자를 표시하여야 합니다.



비영리. 귀하는 이 저작물을 영리 목적으로 이용할 수 없습니다.



변경금지. 귀하는 이 저작물을 개작, 변형 또는 가공할 수 없습니다.

- 귀하는, 이 저작물의 재이용이나 배포의 경우, 이 저작물에 적용된 이용허락조건을 명확하게 나타내어야 합니다.
- 저작권자로부터 별도의 허가를 받으면 이러한 조건들은 적용되지 않습니다.

저작권법에 따른 이용자의 권리는 위의 내용에 의하여 영향을 받지 않습니다.

이것은 [이용허락규약\(Legal Code\)](#)을 이해하기 쉽게 요약한 것입니다.

[Disclaimer](#)

공학박사 학위논문

**Development of Heteroatom-doped  
Graphene and Boron Nitride  
Catalysts for the Application to CO  
Hydrogenation and Selective  
Oxidation of Methane**

이원자가 도핑된 그래핀 및 보론나이트라이드  
촉매의 일산화탄소 수소화반응과 메탄 선택적  
산화반응으로의 응용

2018년 2월

서울대학교 대학원

화학생물공학부

박 홍 석

## Abstract

# **Development of Heteroatom-doped Graphene and Boron Nitride Catalysts for the Application to CO Hydrogenation and Selective Oxidation of Methane**

Hongseok Park

School of Chemical and Biological Engineering

The Graduate School

Seoul National University

Enormous effort has been undertaken for the development of efficient catalyst to achieve low cost and high productivity of chemical process. As the outstanding influence of interrelation between metal and supports is revealed the support materials have been focused by many studies. Among various materials, graphene and boron nitride, which has graphene-analogous structure, have drawn massive attention due to many opportunities in heterogeneous catalysis. The studies referred to herein, contain design of effective catalysts by introducing heteroatoms into graphene and boron nitride.

Optimizing the properties of a catalyst to obtain a desired level of catalytic activity is the goal of heterogeneous catalysis. Here, we tuned the catalytic activity via manipulating the electronic state of a catalyst, induced by facile doping method into graphene at metal/graphene system. Experimental results revealed that the electronic state of the catalyst was manipulated depending on the type, concentration, and doping structure of dopants. For CO

hydrogenation reaction, the catalytic activities of metal/doped graphene catalysts were controlled toward increasing or decreasing way, up to 7.7 times, according to the electronic state of cobalt metal. It was revealed that change in the electronic state led to variations in the interactions between active metal and reactants by kinetic study and theoretical calculations, causing differences in catalytic performances. This strategy was proven to be applicable to not only transition metal and but also noble metal in other reaction such as 4-nitrophenol reduction.

The selective oxidation of methane is one of the most attractive and challenging process in the chemical industry. Here, we synthesized boron nitride (BN)-based catalysts containing atomically dispersed Fe site by means of pyrolytic method. The isolated single Fe sites were distributed throughout defective BN which consists of the typical  $B_3N_3$  hexagonal structure but randomly oriented layers. The unprecedented catalyst, Fe-embedded BN (0.8Fe-BN), exhibited remarkable methane conversion (27%) and formaldehyde selectivity (52%) at 873 K. In comparison with Fe nanoparticle, the single Fe site, which is coordinated to oxygen atoms in square-pyramidal structure, dominantly served as the crucial active site and contributed to the enhanced catalytic performance. These results may provide more opportunities for the use of BN materials for heterogeneous catalysis.

**Keywords:** Heterogeneous catalyst, single atom catalyst, methane, selective oxidation, doping, electronic state, graphene, hydrogenation.

**Student Number:** 2014-31078

# Contents

<b>Chapter 1. Introduction.....</b>	<b>1</b>
1.1 Graphene and boron nitride materials in heterogeneous catalysis .....	1
1.2 Effects of tunable electronic properties on catalytic activity ...	3
1.3 Design of single atom catalyst for selective oxidation of methane .....	3
1.4. Objectives .....	7
<b>Chapter 2. Tuning effects of electronic state in metal/graphene catalysts for the control of catalytic activity via N- and B-doping into graphene.....</b>	<b>38</b>
2.1 Introduction.....	38
2.2 Experimental .....	41
2.2.1 Preparation catalysts .....	41
2.2.2 Characterization .....	41
2.2.3 Catalytic activity test .....	42
2.3 Results and discussion .....	44
2.3.1 Preparation and physicochemical properties of the catalysts	44
2.3.2 Electronic state of doped graphene and active metals.....	16
2.3.3 Reaction tests.....	19
2.3.4 Model reaction tests.....	22
<b>Chapter 3. Selective oxidation of methane over Fe-</b>	

<b>embedded boron nitride catalysts .....</b>	<b>38</b>
<b>3.1 Introduction.....</b>	<b>38</b>
<b>3.2 Experimental .....</b>	<b>41</b>
3.2.1 Preparation of catalysts .....	41
3.2.2 Characterization methods .....	41
3.2.3 Measurements of catalytic performance .....	42
<b>3.3 Results and discussion .....</b>	<b>44</b>
3.3.1 Structural characterization .....	44
3.3.2 Atomically dispersed Fe species within boron nitride.....	48
3.3.3 Catalytic performance over Fe@BN catalysts .....	49
<b>Chapter 4. Summary and Conclusions .....</b>	<b>74</b>
<b>Bibliography .....</b>	<b>76</b>
<b>국 문 초 록 .....</b>	<b>83</b>

# List of Tables

Table 2-1. Physicochemical properties of the prepared Co/N-graphene, Co/undoped-graphene, and Co/B-graphene samples.....	24
Table 2-2. The amounts (at.%) of pyridinic, pyrrolic, and quaternary N in Co/N-graphene samples, and borinic, boronic, and substitutional B in Co/B-graphene samples.....	25
Table 2-3. G-bands of Co/N-graphene, Co/undoped-graphene, and Co/B-graphene at different annealing temperatures, and the corresponding differences ( $\Delta$ ) between supports and catalysts ....	26
Table 2-4. Kinetic parameters for the CO hydrogenation over Co/N-graphene(900), Co/undoped-graphene, and Co/B-graphene(700), as calculated by the best fitted curves.....	27
Table 3-1. Elemental composition (atom% from XPS) of BN, 0.8Fe@BN, and 2.4Fe@BN .....	52

## List of Figures

- Figure 2-1. N<sub>2</sub> adsorption-desorption isotherms of the prepared samples ..... 28
- Figure 2-2. TEM images of a) Co/N-graphene(900), b) Co/N-graphene(800), c) Co/N-graphene(700), d) Co/undoped-graphene, e) Co/B-graphene(700), f) Co/B-graphene(800), and g) Co/B-graphene(900). Scale bar, 50 nm..... 29
- Figure 2-3. XRD patterns of the prepared catalysts..... 30
- Figure 2-4. XPS spectra of N 1s for a) Co/N-graphene(700), b) Co/N-graphene(800), and c) Co/N-graphene(900), and B 1s for d) Co/B-graphene(700), e) Co/B-graphene(800), and f) Co/B-graphene(900)..... 31
- Figure 2-5. XPS spectra of Co 2p for Co/N-graphene, Co/undoped-graphene, and Co/B-graphene, which were prepared at different annealing temperatures. .... 32
- Figure 2-6. Specific activity of CO hydrogenation over Co/B-graphene, Co/undoped-graphene, and Co/N-graphene at different annealing temperatures. 0.1 g of catalyst, [CO/H<sub>2</sub>/N<sub>2</sub>/He] = [7.3/14.6/7.3/70.8], 41 mL/min of total flow, 450 °C of reaction temperature..... 33
- Figure 2-7. TEM images of a) Pd/N-graphene(700), b) Pd/undoped-graphene, and c) Pd/B-graphene(700). .... 34
- Figure 2-8. XRD patterns of Pd/N-graphene(700), Pd/undoped-graphene, Pd/B-graphene(700). .... 35
- Figure 2-9. Pd 3d spectra of Pd/N-graphene(700), Pd/undoped-graphene, and Pd/B-graphene(700). .... 36
- Figure 2-10. Plot of ln(A/A<sub>0</sub>) versus time for the 4-nitrophenol reduction over N-graphene(700), undoped-graphene, B-graphene(700), Pd/N-graphene(700), Pd/undoped-graphene, and Pd/B-graphene(700).

	Reaction condition: 0.1 mg of catalyst, 5.6 mM of NaBH <sub>4</sub> , 0.112 mM of 4-nitrophenol, and 25 °C. ....	37
Figure 3-1.	High-resolution TEM images of (a, b) BN, (c, d) 0.8Fe@BN, and (e, f) 2.4Fe@BN.....	53
Figure 3-2.	Aberration-corrected TEM images of (a, b) BN, (c, d) 0.8Fe@BN, and (e, f) 2.4Fe@BN.....	54
Figure 3-3.	SEM images of (a) BN, (b) 0.8Fe@BN, and (c) 2.4Fe@BN.....	55
Figure 3-4.	High-resolution TEM images of 2.4Fe@BN. The Fe nanoparticles and defects of BN are marked by white arrows and red circles, respectively .....	56
Figure 3-5.	High-resolution TEM images of 0.8Fe@BN (a, b) and 2.4Fe@BN (c, d) after O <sub>2</sub> treatment at 650 °C for 3h.....	57
Figure 3-6.	STEM images of a) BN, b) 0.8Fe@BN, and c) 2.4Fe@BN in the dark field mode and the elemental mapping images of B, N, O, and Fe. Scale bar, 500 nm .....	58
Figure 3-7.	XRD patterns of BN, 0.8Fe@BN, and 2.4Fe@BN.....	59
Figure 3-8.	XRD patterns of 4Fe@BN and 8Fe@BN .....	60
Figure 3-9.	Attenuated total reflectance FT-IR measurement of BN, 0.8Fe@BN, and 2.4Fe@BN.....	61
Figure 3-10.	Attenuated total reflectance FT-IR measurement of 4Fe@BN and 8Fe@BN.....	62
Figure 3-11.	XPS spectra of (a) B 1s, (b) N 1s, and c) O 1s for BN, 0.8Fe@BN, and 2.4Fe@BN.....	63
Figure 3-12.	XPS spectra of Fe 2p for 0.8Fe@BN and 2.4Fe .....	64
Figure 3-13.	Fe K-edge x-ray absorption near-edge structure (XANES) spectra of Fe@BN catalysts with various Fe content in comparison to Fe foil and Fe <sub>2</sub> O <sub>3</sub> .....	65
Figure 3-14.	Fourier transform (FT) extended X-ray absorption fine structure (EXAFS) signals of Fe@BN catalysts with various Fe content in	

comparison to Fe foil and Fe <sub>2</sub> O <sub>3</sub> .....	66
Figure 3-15. Methane conversion over the prepared catalysts (0.05 g) at 873 K compared with 0.8 wt% FeO <sub>x</sub> /SBA-15. FeO <sub>x</sub> /SBA-15 is a well-known catalyst for this reaction so it has been chosen for the comparison. Flow rate : CH <sub>4</sub> (10 ml/min), O <sub>2</sub> (2 ml/min), He (8 ml/min), and N <sub>2</sub> (3 ml/min).....	67
Figure 3-16. Product selectivity over the prepared catalysts (0.05 g) at 873 K compared with 0.8 wt% FeO <sub>x</sub> /SBA-15. FeO <sub>x</sub> /SBA-15 is a well-known catalyst for this reaction so it has been chosen for the comparison. Flow rate : CH <sub>4</sub> (10 ml/min), O <sub>2</sub> (2 ml/min), He (8 ml/min), and N <sub>2</sub> (3 ml/min).....	68
Figure 3-17. Space time yield (STY) of formaldehyde at 873 K over prepared samples compared with 0.8 wt% FeO <sub>x</sub> /SBA-15.....	69
Figure 3-18. Dependence of methane consumption rate over 0.8Fe@BN on partial pressure of a) oxygen (P <sub>oxygen</sub> ) and b) methane (P <sub>methane</sub> ). He was used to balance the total pressure (P <sub>total</sub> : 1atm) .....	70
Figure 3-19. Schematic illustration for the selective oxidation of methane over a) single Fe site of Fe@BN catalysts and b) B-O terminals of BN material.....	71
Figure 3-20. Effect of oxygen partial pressure (P <sub>oxygen</sub> ) over 0.8Fe@BN on product selectivity. T = 873 K, P <sub>methane</sub> = 0.43 atm.....	72
Figure 3-21. Effect of methane partial pressure (P <sub>methane</sub> ) over 0.8Fe@BN on product selectivity. T = 873 K, P <sub>oxygen</sub> = 0.17 atm.....	73

# **Chapter 1. Introduction**

## **1.1 Graphene and boron nitride materials in heterogeneous catalysis**

Enormous endeavors have been undertaken to develop low-cost, highly active, and selective catalysts in order to cut costs and improve the efficiency of process in chemical industry. In consideration of the motivation, precious metals such as Pt, Au, and Pd or their alloys, which act as active sites, are always the first candidate group to enhance catalytic performance in heterogeneous catalysis because they have shown inimitable catalytic activity beyond many other catalytic materials [1-3]. However, all of the precious-metal catalysts are literally rare due to the limited reserves therefore they are not suitable for large-scale industrial applications. Hence, development of efficient catalysts employing nonprecious-metal has become unavoidable issues in this field, including enhancement of precious-metal catalysts to more competent [4-6].

In this context, outstanding influence of supports on the activity of metal nanoparticles, which has been reported recently, leads to focus on the support materials. The interrelation between metal and supports could be used to tune the properties of metal or to disperse active metal atomically. Among a number of support materials, graphene and graphene-analogous materials (boron nitride and metal dichalcogenides) have drawn intensive

attentions due to their characteristic structure [7-9]. The high surface area, thermal stability, high resistance to chemicals, and various electronic properties are fascinating enough to exploit in various fields including heterogeneous catalysis. Above all, the well-defined hexagonal structure of graphene and graphene-like materials has many possibilities to modify physicochemical and electronic properties by introducing heteroatom into the structure. Furthermore, the defective or disordered structure of the graphene and graphene-like materials can be easily functionalized and provide specific site for anchoring active metal atoms [10,11]. These features may open up more opportunities to enhance the activity, selectivity, and durability in heterogeneous catalysis.

## **1.2 Effects of tunable electronic properties on catalytic activity**

Metal nanoparticles dispersed on various support materials have been numerously studied and widely employed in the modern chemical industry. For the development of new catalysts with high activity, identification of major factors determining catalytic performance has been continually pursued. In this context, tuning electronic properties has emerged as a principal issue due to its paramount importance to enhance catalytic activity and fundamental understanding of metal nanoparticle catalysts [12,13]. Among the various strategies to control electron state of metal nanocatalysts, support material is considered a key factor to enhance catalytic performance since the introduction of the effect of the metal-support interaction on catalytic activity [14-16]. According to current insights, the catalytic activity of supported nanoparticles is governed by interrelated physical and chemical properties of metal nanoparticles and support material. Therefore, inducing changes in the interaction or relation between metal and support could be the most promising way to achieve better catalytic effects.

Apart from the transition metal oxide ( $\text{SiO}_2$ ,  $\text{TiO}_2$ , and  $\text{Al}_2\text{O}_3$ ), carbon-based materials, especially graphene, have drawn attention as versatile supports due to the properties such as microporous structure, electrical conductivity, and high stability [17,18]. Above all, tunable chemical and electronic properties

providing a multitude of design possibilities are most fascinating feature of the materials. In spite of the inertness of pure carbon materials, slight modification of the surface can effectively and inevitably induce changes in the properties of the catalytic systems.

### **1.3 Design of single atom catalyst for selective oxidation of methane**

Methane is considered as an alternative resource with high potential because it is the major component of abundant resources such as natural gas and methane hydrates [19]. The readily usable energy source is cleaner than petroleum and coal and offers promising a platform molecules such as syngas. In spite of the favorable features of methane, natural gas is still underutilized due to the high costs for transportation [20]. In this regard, much effort has been devoted to direct methane conversion to produce the desired chemicals, which are economically competitive, in high yields in order to make the usage of methane more viable and practical. Direct conversion of methane into oxygenates has been of crucial importance in chemical industry due to the environmental and economic issues. However, there are challenging aspects in design of catalyst for this reaction and they are to activate C-H bond in methane and to suppress further oxidation of intermediates such as methanol and formaldehyde. To overcome the limitation, single atom catalysts (SACs), which contain individual and isolated metal atoms anchored to support, are considered as promising materials [21,22]. As the size of metal particles on support is reduced, more surface atoms locate in a low-coordination environment and the strong metal-support interaction appears. These surface atoms become more active to specific reactions than its nanoparticle

counterpart [23]. Besides, the fine dispersion of active site throughout support material could contribute to avoid further oxidation of the reactive intermediates.

## 1.4. Objectives

This thesis mainly consists of designing catalysts for the selective oxidation of methane and CO hydrogenation by employing graphene and graphene-analogous material.

In following section, Chapter 2, the opposite effects of heteroatom (N or B) doping in graphene on catalytic activity in CO hydrogenation are shown. The occurrence of enhancement and retardation effects can be related to the changes in electronic state of active metal, which caused by incorporation of N and B in carbon matrix.

In the final part of this thesis, the synthesis of Fe-embedded catalyst by facile pyrolytic method is represented. The prepared catalyst, which is featured by the atomically-dispersed Fe species in boron nitride, is exhibits superior catalytic activity in the selective oxidation of methane to formaldehyde.

# **Chapter 2. Tuning effects of electronic state in metal/graphene catalysts for the control of catalytic activity via N- and B-doping into graphene**

## **2.1 Introduction**

Maximizing catalytic activity is of great importance for energy-efficient process in the chemical industry [24-27]. In heterogeneous catalysis, various approaches have been applied to augment the reactivity of a catalyst. For example, process parameters such as temperature, contact time, pressure, etc. have been optimized to achieve a desired level of catalytic performance [28-30]. In a range from the macro- to nano-scale, shapes, surface areas, and pore sizes of catalysts have been controlled [31-33]. Surface atomic coordination and composition have also been considered at the atomic level [34,35]

Recently, the advances in characterization tools and theoretical calculations allow fundamental understanding for catalysis [36,37] Hence, it has been revealed that electronic structure is one of the important factors to influence its catalytic reactivity [38-39]. For example, core-shell, alloy, size control, surface strain, ligand, confinement, and so on have been used as strategies for achieving the variation in electronic structure of a catalyst [40-45]. However, the approaches change not only the electronic structure of a

catalyst but also other parameters determining catalytic reactivity such as compositions, and the coordination numbers of atoms of active site, etc [46,47]. In addition, for most of approaches to obtain the variation in electronic structure, preparation steps of a catalyst are too complicated, and required high-quality and sophisticated techniques (ex. atomic layer deposition, surfactant-assistant method etc.) [48-50]. Although tuning the electronic structure is effective to enhance catalytic reactivity, there is a lack of facile and effective strategies to manipulate the electronic structure of a catalyst.

Herein, we report a strategy to tune catalytic activity of nano-particles supported on graphene by controlling the electronic state of the active metal. Graphene is a good candidate as a support because its chemical properties can be easily modified [51]. For the variation in electronic state of the catalyst, heteroatoms (N or B) were introduced to graphene with various concentrations and doping structures. Then, active metal was loaded on the doped graphene, which induces a change in the electronic state of the active metal. The variations in the electronic states of the catalysts were confirmed via experimental characterizations and theoretical calculations. It is noteworthy that the catalytic activity of CO hydrogenation was controlled toward not only enhancement but also reduction. Kinetic study and theoretical calculations revealed that the change in the interactions between the active metal and reactants by controlling electronic state affected the catalytic activity. It was proven that the strategy can be applied to not only transition metal but also noble metal in other model reaction (4-nitrophenol

reduction) as well as CO hydrogenation. To the best of our knowledge, this is the first report for revealing opposites effect of N and B as dopants into graphene on both electronic states of active metal and heterogeneous catalysis.

## 2.2 Experimental

### 2.2.1 Preparation of catalysts

Graphene oxide (GO) was prepared via following a procedure reported in a previous study. 1.5 g of Graphite flakes (Sigma-aldrich) was added to admixture of 180 ml of concentrated  $\text{H}_2\text{SO}_4$  ( $\geq 95\%$ , Samchun) and 20 mL of  $\text{H}_3\text{PO}_4$  ( $\geq 85\%$ , Samchun), and 9.0 g of  $\text{KMnO}_4$  (99%, Sigma-aldrich) was then slowly added with vigorous stirring for 12 h at 40 °C. The mixture was cooled to room temperature, and 200 mL of an aqueous  $\text{H}_2\text{O}_2$  solution (190 mL of deionized water and 10 mL of 30 wt.% in  $\text{H}_2\text{O}_2$ ) was then added. The solution stirred for 1 h. The precipitate was then washed with deionized water, HCl (35-37%, Samchun), and ethanol repeatedly. The washed precipitate was coagulated with ether ( $\geq 99\%$ , Sigma–Aldrich). Finally, yellow powder was obtained by vacuum-drying overnight at room temperature.

For the preparation of N-doped graphene (N-graphene), 2 g of GO was heated under an ammonia atmosphere at three different temperatures (700, 800, and 900 °C) for 4 h. The as-obtained samples were denoted as N-graphene(700), N-graphene(800), and N-graphene(900). B-doped graphene (B-graphene) was synthesized by annealing 2 g of GO powder with mixed with excess boric acid under a  $\text{N}_2$  atmosphere at different temperatures (700, 800, and 900 °C) for 4 h. The samples were denoted as B-graphene(700), B-graphene(800), and B-graphene(900). Undoped-graphene was prepared by

annealing 2 g of GO powder under a N<sub>2</sub> atmosphere at 500 °C for 4 h.

The catalysts, which have the constant amount of cobalt (3 wt%) on N-graphene, undoped graphene, and B-graphene (Co/N-graphene, Co/undoped-graphene, and Co/B-graphene), were prepared by following procedure. A 0.3 g of support (N-graphene, undoped-graphene, and B-graphene) was dispersed in an admixture of 15 mL of ethanol ( $\geq 99.5$ , Sigma-Aldrich) and 15 mL of deionized water, which was then sonicated for 1 h. Then, 1 mL of aqueous solution containing the calculated amount of cobalt nitrate hexahydrate (99.999%, Sigma-Aldrich) was added to the support dispersed solution. The solution was further sonicated for 1 h. The solvent was then removed by evaporation under reduced pressure at room temperature, and the resulting solids were dried overnight at 80 °C. The samples were reduced in a stream of 10 vol.% H<sub>2</sub>/He at 550 °C for 3 h. Cube-shaped palladium nanoparticles were synthesized according to a previously described method [S2] Palladium supported on N-graphene(700), undoped-graphene, and B-graphene(700) were prepared by incipient wetness method. The samples were denoted as Pd/N-graphene(700), Pd/undoped-graphene, and Pd/B-graphene(700).

### **2.2.2 Characterization**

XRD patterns of the catalysts were measured by using a Rigaku d-MAX2500-PC powder X-ray diffractometer operating at 50 kV and 100 mA using CuK $\alpha$  radiation (1.5406 Å). High-resolution transmission electron

micrograph (HR-TEM) images were obtained on JEOL JEM-3010 microscope with an acceleration voltage of 300 kV. The N<sub>2</sub> adsorption-desorption isotherms were measured at -196 °C using a Micrometrics ASAP-2010 system. The total surface area of the samples was calculated by the BET method ( $P/P_0=0.05\sim 0.15$ ). Raman spectroscopy was performed on a HORIBA T64000 using a multichannel charge-coupled device (CCD) detector at room temperature. The external laser source was used for excitation, an Ar laser at 514 nm. The loading amount of active metal on support was analyzed by inductively coupled plasma atomic emission spectroscopy (ICP-AES, OPTIMA 4300DV). X-ray photoelectron spectroscopy (XPS) was performed using a Sigma Probe instrument (ThermoVG). The binding energy of each element was calibrated by using the carbon peak as standard (C 1s = 284.5 eV).

### **2.2.3 Catalytic activity test**

The catalytic activity test for CO hydrogenation was carried out at 450 °C under atmospheric pressure. A 0.1 g of powder sample was loaded into a quartz reactor (11 mm inner diameter), the reactor was then placed in an electric furnace. The temperature of the catalyst bed was monitored by a thermocouple and controlled through a PID controller. Before the reaction, the catalyst was preheated to the reaction temperature under a reducing atmosphere (H<sub>2</sub> and N<sub>2</sub>) at 450 °C for 1 h. Total flow was fixed at 41 mL/min. The molar ratio of H<sub>2</sub> to CO was 2. N<sub>2</sub> (3 mL/min) and He (29 mL/min) were

used as an internal standard and a carrier, respectively.

For the reaction kinetic studies, the partial pressures of CO and H<sub>2</sub> (P<sub>CO</sub> and P<sub>H<sub>2</sub></sub>, respectively) were controlled, and Ar was used to balance the total flow (30 mL/min). N<sub>2</sub> (3 mL/min) was injected as an internal standard. The reaction tests were conducted over 0.05 g of catalyst at temperature range of 400-450 °C.

For 4-nitrophenol (4-NP) reduction, 0.1 mg of catalyst was added to an aqueous solution of 5.618 mM of NaBH<sub>4</sub> and 0.112 mM of 4-NP at room temperature. The time dependent reduction was elucidated from the absorbance spectra which were recorded with a Jasco V670 spectrometer.

## **2.3 Results and discussion**

### **2.3.1 Preparation and physicochemical properties of the catalysts**

The physical properties of Co/N-graphene, Co/undoped-graphene, and Co/B-graphene were characterized by BET and ICP analysis. As shown in Figure 2-1, the isotherms of the catalysts exhibited a pseudo type-II pattern, which originated from slit-like open pores [52]. The BET surface areas and pore volumes of the catalysts were increased according to the annealing temperature from 700 °C to 900 °C in the both cases of Co/N-graphene and Co/B-graphene samples (Table 2-1). The weight percent of the Co nanoparticles deposited on the supports was about 3 wt% in all cases.

The particle size of Co in the prepared samples was examined via transmission electron microscopy (TEM) (Figure 2-2). The well dispersed Co nanoparticle was observed in all samples. It is well known that catalytic activity of cobalt nanoparticles for CO hydrogenation depends on the particle size in the small-size range [53-55]. The results of previous researches have shown that catalytic performance increases as the Co nanoparticle size is increased to below 6 nm whereas the influence of particle size is negligible for the particles larger than 6 nm. In this study, the sizes of the Co nanoparticle on N-graphene, undoped-graphene, and B-graphene were shown to be above 6 nm with a narrow distribution despite the differences in surface area among the supports (see inset in Figure 2-2 and Table 2-1). Therefore the particle size was ruled out as a crucial factor for determining

catalytic performance among the samples. The XRD patterns (Figure 2-3) indicate that the cobalt species was present in the metallic phase with corresponding peak ( $2\theta = 44.22^\circ$ , JCPDS 15-0806) [56], and also exhibit similar crystallinity among the catalysts. Thus, it is confirmed that differences in loading amount, size, phase, and crystallinity of active metal are negligible, which indicates that the effects of the parameters on the catalytic activity can be excluded among the catalysts.

### **2.3.2 Electronic state of doped graphene and active metals**

XPS analysis was carried out to reveal how the doping of N and B affects the electronic states of doped graphene materials and the active metals on them. For N-graphene, the N1s spectra (Figure 2-4) were deconvoluted into the different types of nitrogen, which included pyridinic (398.1 eV), pyrrolic (399.5 eV), quaternary center (400.9 eV) and quaternary valley (402.5 eV). The content of N in Co/N-graphene was decreased as the annealing temperature was increased (Table 2-1). In detail, as the annealing temperature was increased, a decreasing trend for pyrrolic and pyridinic N, and an increasing trend for quaternary N species (center and valley) were observed (Table 2-2). For quaternary N, three valence electrons of nitrogen form three  $\sigma$  bonds with the neighboring carbon atoms, one electron is engaged in a  $\pi$  bond formation, and the fifth electron is partially involved in the  $\pi^*$ -state of the conduction band [57]. It was previously reported that quaternary N shifts up Fermi level acting as a n-type dopant while pyridinic

and pyrrolic N decreases Fermi level acting as a p-type dopant [58,61]. Therefore, the Fermi levels of N-graphene were expected to increase from N-graphene(700) to N-graphene(900). The B1s peak for Co/B-graphene also includes three different doping states of boron within graphene: substitutional (190.9 eV), borinic (192.3 eV), and boronic (193.2 eV) (Figure 2-4) [62]. For B-graphene, the concentration of the substitutional doping of the B atom into a graphene framework was increased as the annealing temperature was increased (Table 2-2). Considering that substitutional doping of B atom into graphene is well known as a p-type dopant [63,64] downshift Fermi-level of B-graphene is expected compared with that of undoped-graphene. It is considered that both electron-rich and -deficient supports was induced by chemical doping method.

Further analysis was conducted to investigate how the modified supports have influenced on Co nanoparticles. The Co 2p peak was gradually shifted to a lower level of binding energy from Co/undoped-graphene to Co/N-graphene(900) (Figure 2-5). The opposite shift of Co 2p peak for Co/B-graphene was obtained referring to Co/undoped-graphene. The obvious shift of Co 2p peak demonstrates that the Co nanoparticles have higher electron density for Co/N-graphene and lower electron density for Co/B-graphene than that for Co/undoped-graphene. It is noteworthy that the electronic state of the Co nanoparticles was affected by the chemically heteroatom-doped graphene. A Raman shift of the G-band also supported the change in the electronic states of the catalysts (Table 2-3). The frequency of G-band ( $1500\sim 1600\text{ cm}^{-1}$ ) is sensitive to the charge transfer between metal and

graphene material [65]. When the Co was loaded onto the undoped-graphene, a Raman shift ( $+1.10 \text{ cm}^{-1}$ ) was observed. This was the result of a metal-support interaction via the electron transfer from graphene to Co nanoparticles [66]. For Co/N-graphene, the peak shift became more positive ( $+1.65 \text{ cm}^{-1}$ ) for Co/N-graphene(700), and it was further increased to  $+7.71 \text{ cm}^{-1}$  for Co/N-graphene(900). The increased shift of G-band indicates that more electrons of the graphene-based supports were transferred to the Co nanoparticles. On the other hand, the G-bands of the Co/B-graphene samples appeared at lower frequencies compared to that of the Co/undoped-graphene. The shift became more negative from Co/undoped-graphene to Co/B-graphene(900), which implies that the direction of the charge transfer between the Co nanoparticles and B-graphene was opposite that of the Co/undoped-graphene samples.

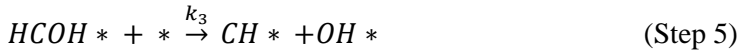
Contrary to Co/undoped-graphene and Co/N-graphene systems, in the case of Co/B-graphene, electron transfer occurs in the opposite direction from Co to B-graphene. Consequently, the electron density of Co on B-graphene is decreased. A positive shift of binding energy in XPS and a negative G-band shift in the Raman spectrum support the schematic diagram of Co/B-graphene system. Based on the comprehensive characterizations, it was confirmed that the electronic state of the active metals was manipulated by this facile chemical doping method with variations in the types, structures, and concentrations of the dopants.

### 2.3.3 Reaction tests

With the intended modification in electronic structure by hetero-atom doping, catalytic performances of the Co/doped graphene catalysts were evaluated in CO hydrogenation as a model reaction (Figure 2-6). As the obvious differences observed in the position of Co 2p peak above, the differences in the specific activity were even clearer. The specific activity for CO hydrogenation was increased from Co/undoped-graphene to Co/N-graphene(900), exhibiting 7.7 times higher activity for Co/N-graphene(900) compared with that for Co/undoped-graphene. On the other hand, a decreasing trend in the specific activity was observed from Co/undoped-graphene to Co/B-graphene(900). It is noteworthy that a considerably low specific activity was obtained with Co/B-graphene(900) despite the negligible differences in physicochemical properties (particle size, phase, loading amount of Co, etc.) compared with Co/N-graphene and Co/undoped-graphene. We also confirmed that the catalysts without Co (N-graphene, undoped-graphene, and B-graphene) exhibited no catalytic activity. These results imply that the high specific activity is obtained when Co nanoparticles exhibit high electron density where Co nanoparticles with low electron density lead to low specific activity. Therefore, we confirmed that the catalytic activity was controlled by manipulation of the electronic state of active metal via facile chemical doping method.

To gain kinetic insights according to the electronic state of the catalysts, we measured the reaction rate according to the various partial pressures of the reactants ( $P_{\text{CO}}$  and  $P_{\text{H}_2}$ ). As model catalysts for each system, we chose Co/N-graphene(900), Co/undoped-graphene, and Co/B-graphene(700).

Although controversies remain concerning the CO dissociation pathway, it was demonstrated that the CO dissociation on cobalt nanoparticle is assisted by hydrogen. The Langmuir-Hinshelwood (LH) rate expression for CO conversion is derived the assumption of CO dissociation pathway assisted by hydrogen. The steps of hydrogen assisted CO dissociation pathway are below.



Assume that steps (1 to 3) are quasi-equilibrium and step 4 is considered as a rate determining step for CO conversion.

$$\theta_H = \sqrt{K_{H_2} P_{H_2} \theta_*}$$

$$\theta_{CO} = K_{CO} P_{CO} \theta_*$$

Pseudo steady-state for HCO\* species

$$k_1 \theta_{CO} \theta_H - k_{-1} \theta_{HCO} \theta_* = 0$$

$$\theta_{HCO} = K_1 K_{CO} P_{CO} \sqrt{K_{H_2} P_{H_2} \theta_*}$$

$$-r_{CO} = k_2 \theta_{HCO} \theta_H = k_2 K_1 K_{CO} K_{H_2} P_{CO} P_{H_2} \theta_*^2$$

$$\theta_* + \theta_{CO} + \theta_H + \theta_{HCO} = 1$$

$$\theta_* = \frac{1}{1 + K_{CO} P_{CO} + \sqrt{K_{H_2} P_{H_2}} + K_1 K_{CO} P_{CO} \sqrt{K_{H_2} P_{H_2}}}$$

Assume that CO\* and \* are the most abundant reaction intermediate based

on the reaction results. The high coverage of adsorbed CO molecules on the surface is considered to hinder the conversion of CO. Therefore, the above expression can be simplified as below.

$$\theta_* = \frac{1}{1 + K_{CO}P_{CO}}$$

$$-r_{CO} = k_2\theta_{HCOH}\theta_* = \frac{k_2K_1K_{H_2}K_{CO}P_{CO}P_{H_2}}{(1 + K_{CO}P_{CO})^2}$$

$$-r_{CO} = \frac{k_{app}K_{CO}P_{CO}P_{H_2}}{(1+K_{CO}P_{CO})^2}$$

where  $-r_{CO}$  is the rate of CO conversion,  $P_{CO}$  is the CO partial pressure,  $P_{H_2}$  is the H<sub>2</sub> partial pressure, and the parameters  $k_{app}$  and  $K_{CO}$  represent an apparent rate constant and the CO adsorption constant, respectively.

The similar dependencies of CO conversion rate over the catalysts on the partial pressure of CO and H<sub>2</sub> are observed. The CO consumption rate began to decrease after reaching its maximum as increasing CO partial pressure with fixed H<sub>2</sub> partial pressure. Under conditions of constant CO partial pressure, a linear relationship was observed between CO conversion rate and the variation of H<sub>2</sub> partial pressure. It suggests that the high coverage of adsorbed CO molecules on the surface hindered the conversion of CO whereas the increasing availability of H on the catalytic surface contributed to increase in the rate of CO conversion [70]. The catalytic reaction results for the catalysts followed Equation S1, which is derived with assumption of CO dissociation pathway assisted by hydrogen. These kinetic behaviors clearly demonstrated no change in the reaction mechanism of the catalysts.

The effect of the N and B-doping into graphene on the CO conversion rate is shown by the kinetic parameters  $k_{app}$  and  $K_{CO}$  in Table 2-4. Compared to

Co/undoped-graphene, the higher value of  $k_{app}$  for the Co/N-graphene(900) catalyst indicates that electron-rich Co could facilitate CO dissociation in the presence of hydrogen, which is considered as the rate-determining step [70,71] On the other hand, Co/B-graphene(700) exhibited a lower value of  $k_{app}$  than Co/undoped-graphene. Considering the values of  $K_{CO}$ , the inhibition effect of high CO coverage on CO consumption rate over Co/undoped-graphene and Co/B-graphene(700) was possibly revealed through the high magnitude of  $K_{CO}$  within a given range of temperature. Based on the results, the electron-abundant state of Co nanoparticles favored CO dissociation assisted by hydrogen and the electron-deficient state of nanoparticles led to the molecular adsorption of CO, resulting in the hindrance of CO conversion.

### **2.3.4 Model reaction tests**

For the broader applications of this facile method, we performed experiment for another reaction (4-nitrophenol reduction) with different active metal (Pd). As with Co/doped graphene systems, highly dispersed Pd nanoparticles on the support materials and the metallic phase were observed in TEM images and XRD patterns, respectively (Figure 2-7 and 2-8). Compared to the undoped and B-doped counterparts, the Pd 3d peak of Pd/N-G(700) was shifted to a lower binding energy region, which indicates the electron-rich state of the Pd surface species (Figure 2-9). In that, electron density of Pd was manipulated depending on the type of supports. As we expected, the activities were controlled, and ordered as Pd/B-G(700) >

Pd/un-G > Pd/N-G(700) in Figure 2-10. This can be explained by modifying the electron density of Pd through the electron transfer between Pd and the doped graphenes. From the mechanistic point of view, 4-nitrophenol forms 4-nitrophenolate via deprotonation. The negatively charged ions ( $\text{BH}_4^-$  and 4-nitrophenolate) are preferentially adsorbed onto the electrophilic Pd on B-G compared to Pd on un-G and N-G [73,74]. From these results, it was confirmed that the catalytic activity was controlled by the electronic state of not only transition metal but also noble metal catalyst via our facile method, proving this strategy applicable to various catalytic systems.

**Table 2-1.** Physicochemical properties of the prepared Co/N-graphene, Co/undoped-graphene, and Co/B-graphene samples.

	$D_{ave}$ <sup>a</sup>	N content <sup>b</sup> (at.%)	B content <sup>b</sup> (at.%)	Co content <sup>c</sup> (wt.%)	BET surface area <sup>d</sup> (m <sup>2</sup> /g)	Pore volume <sup>e</sup> (cm <sup>3</sup> /g)
Co/N-graphene(900)	8.6	4.31	-	3.26	371.3	0.402
Co/N-graphene(800)	9.0	5.77	-	2.97	305.2	0.265
Co/N-graphene(700)	8.4	5.97	-	2.96	127.7	0.241
Co/undoped-graphene	8.6	-	-	3.27	74.5	0.106
Co/B-graphene(700)	9.0	-	1.05	3.28	152.8	0.329
Co/B-graphene(800)	8.8	-	0.94	3.23	248.0	0.464
Co/B-graphene(900)	8.7	-	1.49	3.04	239.8	0.534

<sup>a</sup> $D_{ave}$  indicates average sizes of Co nanoparticle on N-G, un-G, and B-G samples, measured based on each TEM image.

<sup>b</sup>N and B contents in the catalysts were measured by XPS analysis.

<sup>c</sup>Loading weight percent of Co was analyzed by ICP analysis.

<sup>d</sup>The Brunauer–Emmett–Teller (BET) surface area was determined from the N<sub>2</sub> adsorption branch in the relative pressure range from 0.05 to 0.12.

<sup>e</sup>Total pore volume ( $V_{total}$ ) was evaluated at a relative pressure of 0.99.

**Table 2-2.** The amounts (at.%) of pyridinic, pyrrolic, and quaternary N in Co/N-graphene samples, and borinic, boronic, and substitutional B in Co/B-graphene samples.<sup>a</sup>

	Pyridinic N	Pyrrolic N	Quaternary N
Co/N-G(700)	3.45	1.63	1.56
Co/N-G(800)	3.29	1.47	1.63
Co/N-G(900)	2.39	0.65	1.81
	Borinic B	Boronic B	Substitutional B
Co/B-G(700)	0.56	0.11	0.25
Co/B-G(800)	0.37	0.11	0.34
Co/B-G(900)	0.33	0.37	0.60

<sup>a</sup>The compositions of N and B were determined by XPS.

**Table 2-3.** G-bands of Co/N-graphene, Co/undoped-graphene, and Co/B-graphene at different annealing temperatures, and the corresponding differences ( $\Delta$ ) between supports and catalysts.

Catalyst	G-band peak ( $\text{cm}^{-1}$ )	$\Delta$ ( $\text{cm}^{-1}$ )
N-graphene(900)	1591.21	+7.71
Co/N-graphene(900)	1598.92	
N-graphene(800)	1592.31	+4.41
Co/N-graphene(800)	1596.72	
N-graphene(700)	1594.52	+1.65
Co/N-graphene(700)	1596.17	
undoped-graphene	1595.07	+1.1
Co/undoped-graphene	1596.17	
B-graphene(700)	1595.62	-0.55
Co/B-graphene(700)	1595.07	
B-graphene(800)	1596.17	-3.31
Co/B-graphene(800)	1592.86	
B-graphene(900)	1596.72	-6.06
Co/B-graphene(900)	1590.66	

**Table 2-4.** Kinetic parameters for the CO hydrogenation over Co/N-graphene(900), Co/undoped-graphene, and Co/B-graphene(700), as calculated by the best fitted curves.

Catalyst	T (°C)	$k_{app}$ ( $\text{mol}_{\text{CO}} \cdot \text{g}_{\text{cat}}^{-1} \cdot \text{min}^{-1} \cdot \text{atm}^{-1}$ )	$K_{\text{CO}}$ ( $\text{atm}^{-1}$ )
Co/N-graphene(900)	400	$3.70 \times 10^{-2}$	3.27
	425	$5.64 \times 10^{-2}$	1.99
	450	$8.10 \times 10^{-2}$	1.53
Co/undoped-graphene	400	$1.65 \times 10^{-2}$	6.27
	425	$2.49 \times 10^{-2}$	5.97
	450	$3.66 \times 10^{-2}$	5.52
Co/B-graphene(700)	400	$1.51 \times 10^{-2}$	10.82
	425	$2.16 \times 10^{-2}$	9.29
	450	$3.33 \times 10^{-2}$	8.86

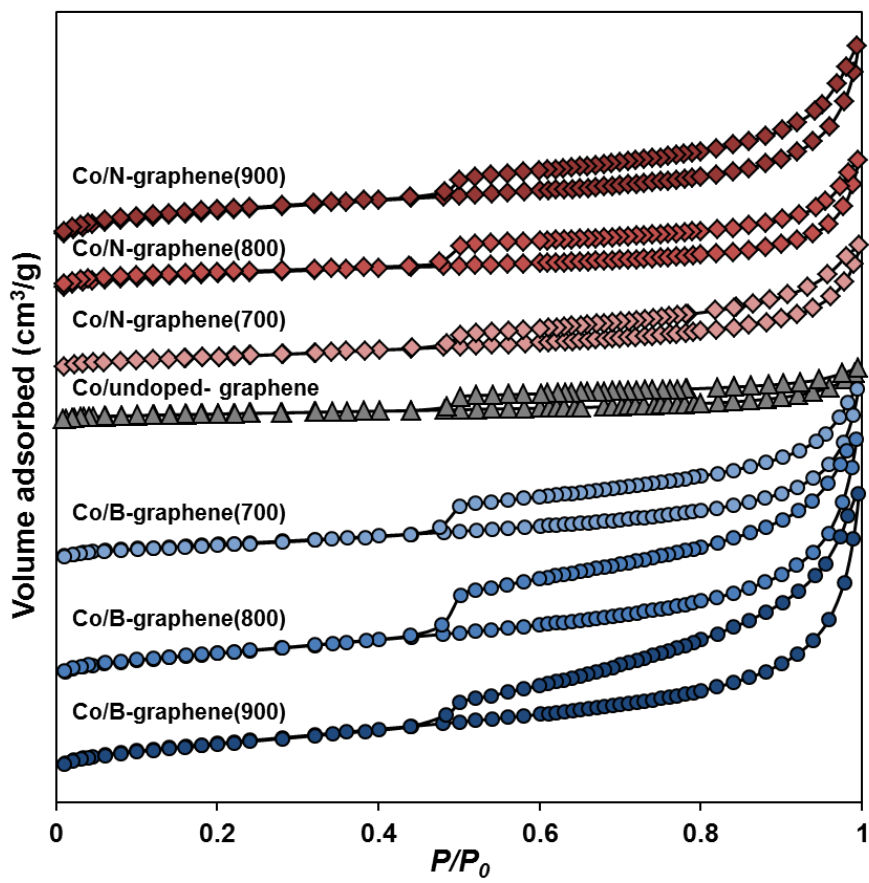
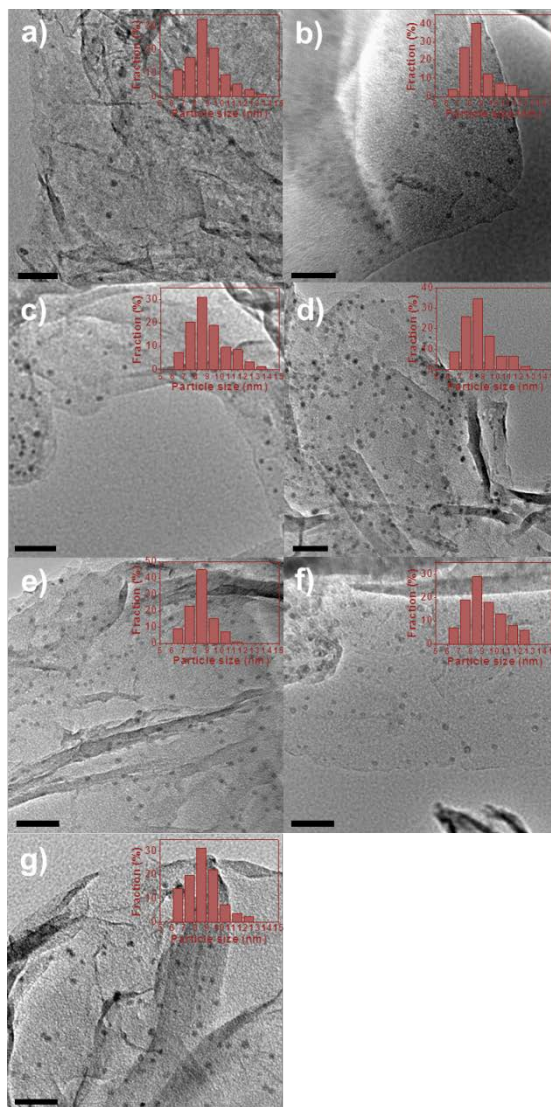


Figure 2-1. N<sub>2</sub> adsorption-desorption isotherms of the prepared samples.



**Figure 2-2.** TEM images of a) Co/N-graphene(900), b) Co/N-graphene(800), c) Co/N-graphene(700), d) Co/undoped-graphene, e) Co/B-grapehen(700), f) Co/B-graphene(800), and g) Co/B-graphene(900). Scale bar, 50 nm.

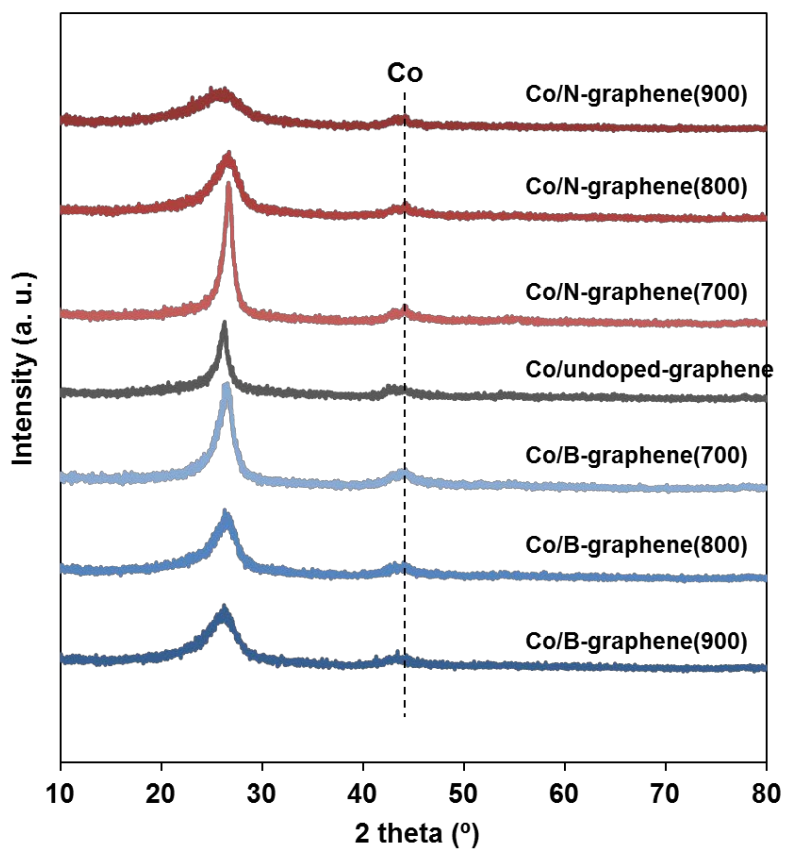
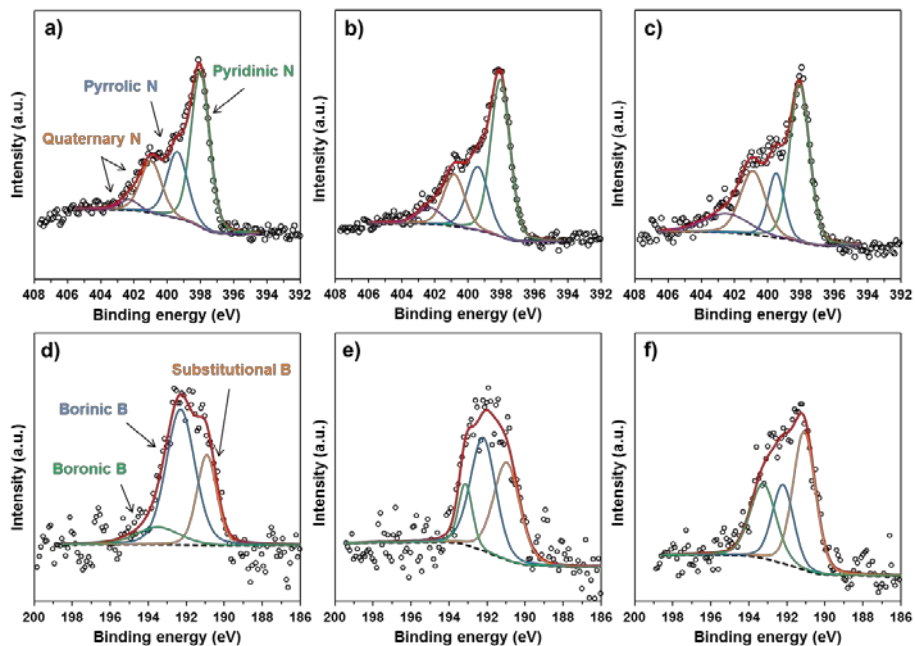
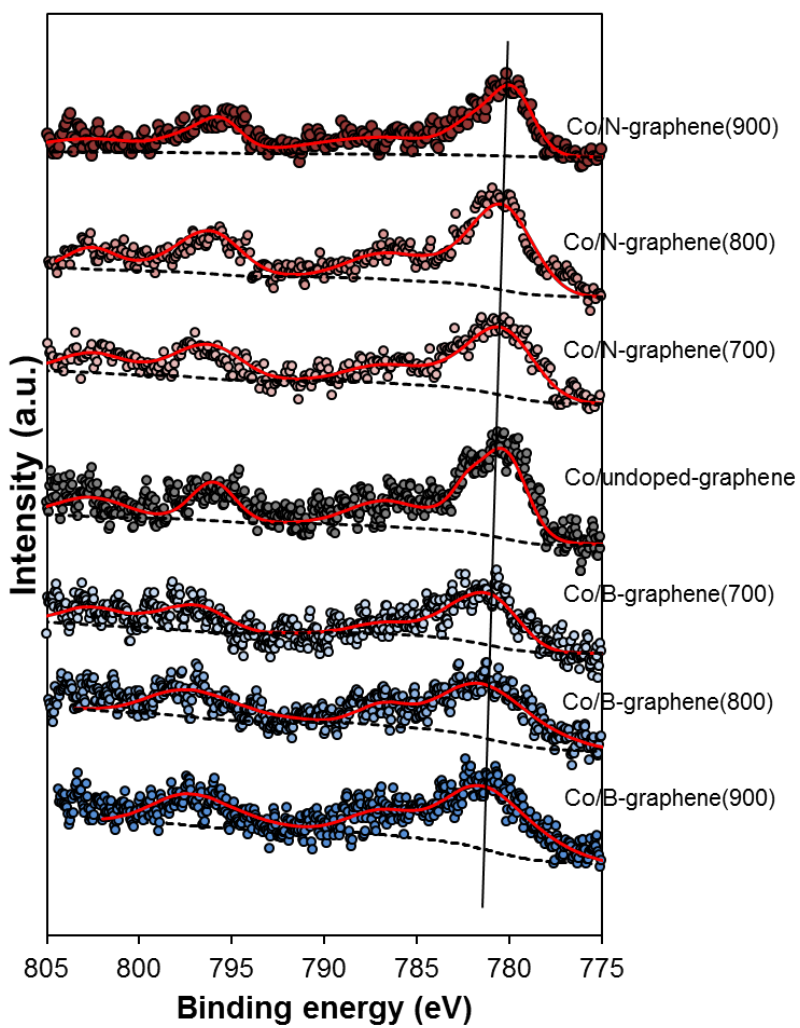


Figure 2-3. XRD patterns of the prepared catalysts.



**Figure 2-4.** XPS spectra of N 1s for a) Co/N-graphene(700), b) Co/N-graphene(800), and c) Co/N-graphene(900), and B 1s for d) Co/B-graphene(700), e) Co/B-graphene(800), and f) Co/B-graphene(900).



**Figure 2-5.** XPS spectra of Co 2p for Co/N-graphene, Co/undoped-graphene, and Co/B-graphene, which were prepared at different annealing temperatures.

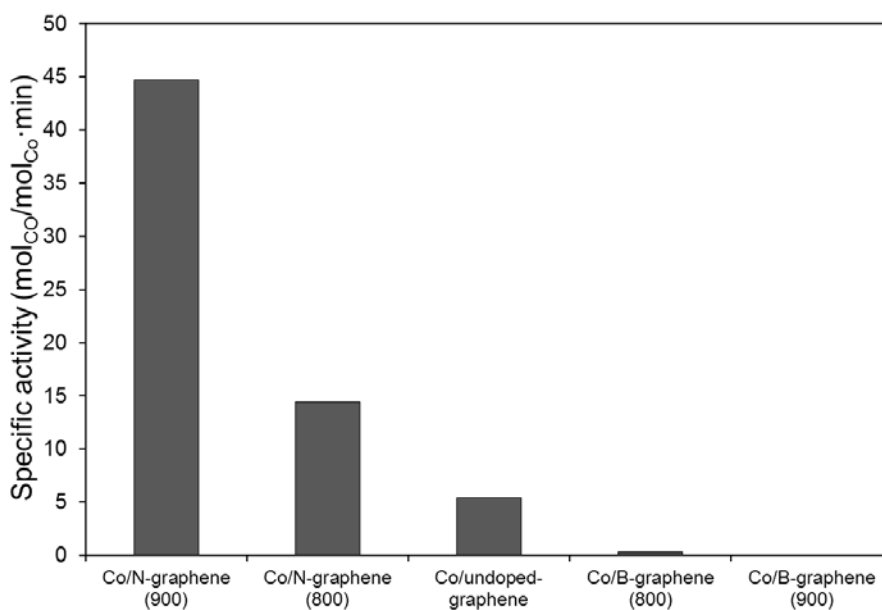


**Figure 2-6.** Specific activity of CO hydrogenation over Co/B-graphene, Co/undoped-graphene, and Co/N-graphene at different annealing temperatures. 0.1 g of catalyst, [CO/H<sub>2</sub>/N<sub>2</sub>/He]=[7.3/14.6/7.3/70.8], 41 mL/min of total flow, 450 °C of reaction temperature.

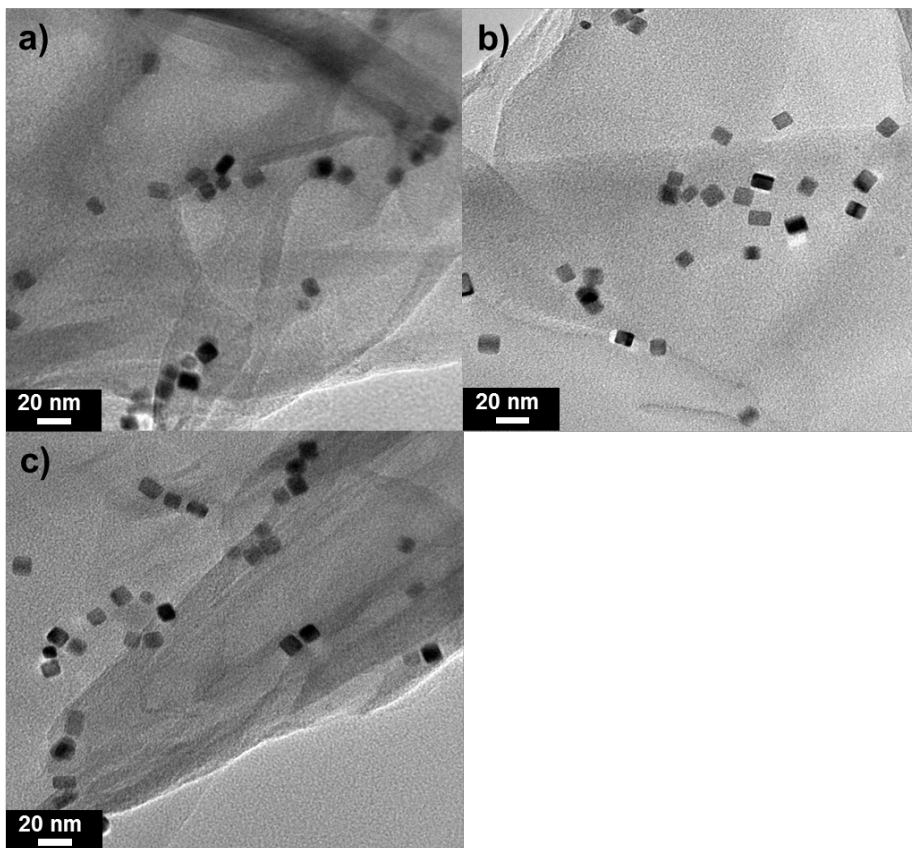


**Figure 2-7.** TEM images of a) Pd/N-graphene(700), b) Pd/undoped-graphene, and c) Pd/B-graphene(700)

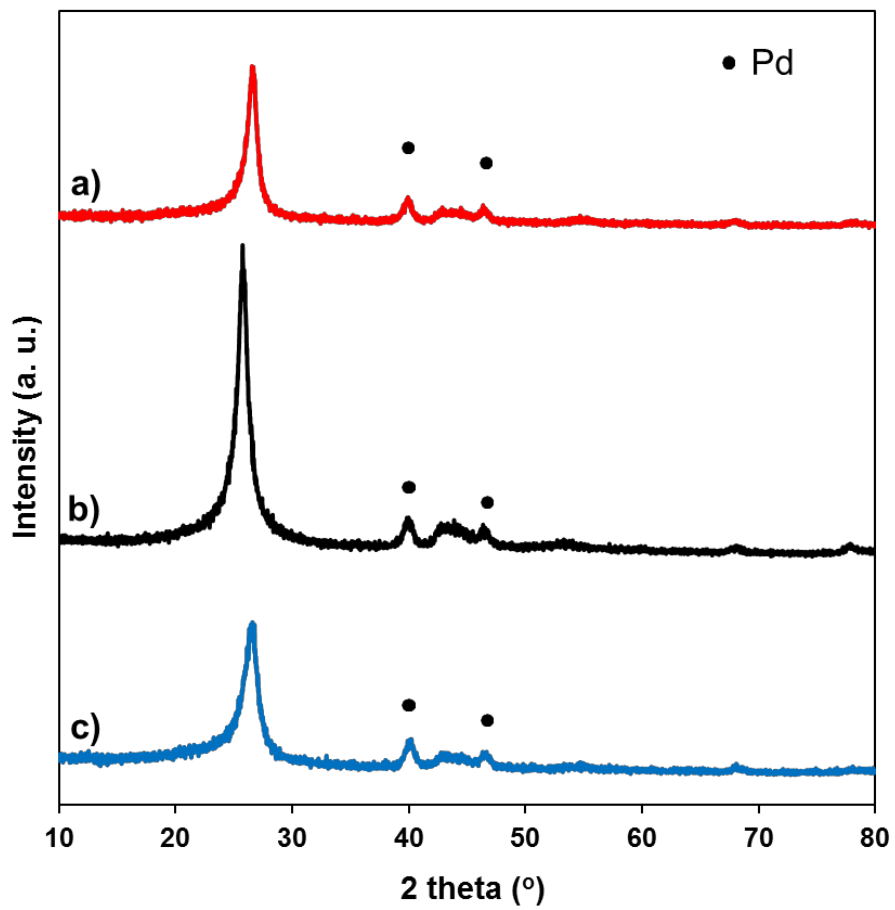


**Figure 2-8.** XRD patterns of Pd/N-graphene(700), Pd/undoped-graphene, Pd/B-graphene(700).

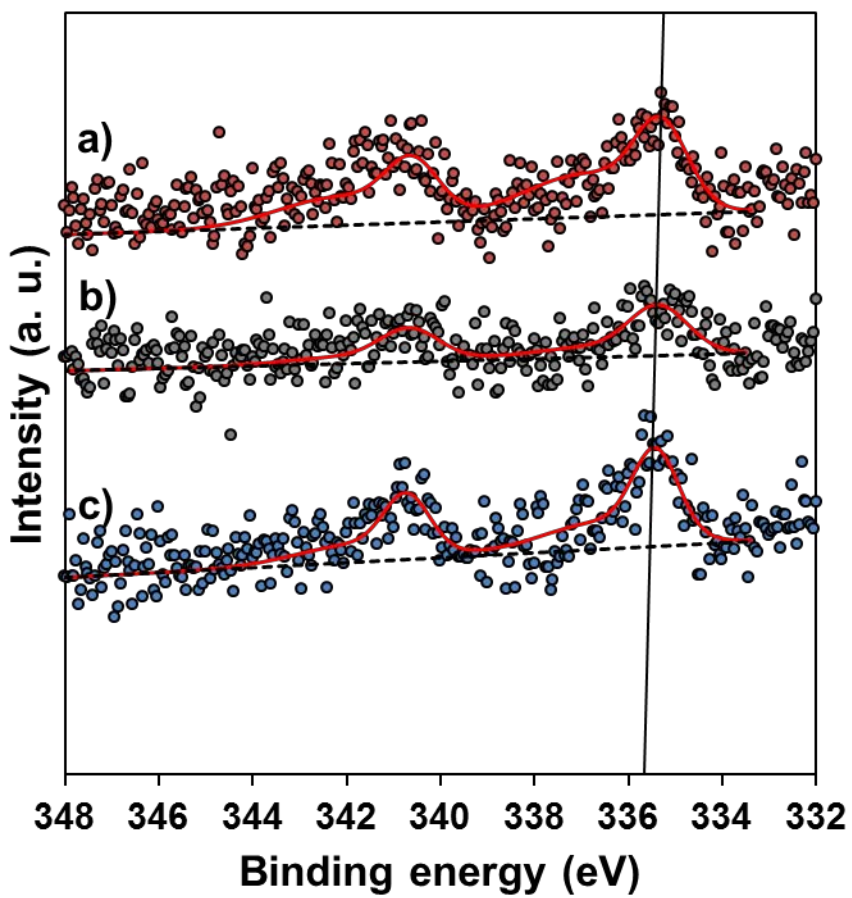


**Figure 2-9.** Pd 3d spectra of Pd/N-graphene(700), Pd/undoped-graphene, and Pd/B-graphene(700).

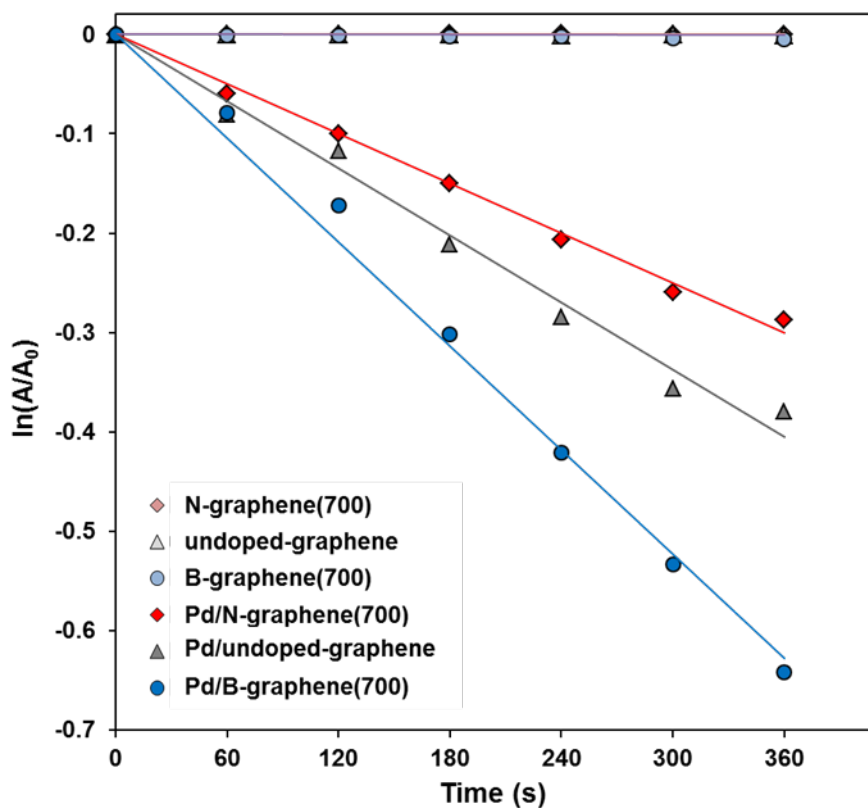


**Figure 2-10.** Plot of  $\ln(A/A_0)$  versus time for the 4-nitrophenol reduction over N-graphene(700), undoped-graphene, B-graphene(700), Pd/N-graphene(700), Pd/undoped-graphene, and Pd/B-graphene(700). Reaction condition: 0.1 mg of catalyst, 5.6 mM of  $\text{NaBH}_4$ , 0.112 mM of 4-nitrophenol, and 25 °C.

# **Chapter 3. Selective oxidation of methane over Fe-embedded boron nitride catalysts**

## **3.1 Introduction**

In the modern chemical industry, catalytic selective oxidation of hydrocarbons is a crucial technology, allowing the production of fuels and chemicals [75,76]. Among various partial oxidation reactions, direct conversion of methane into oxygenates has drawn massive attention due to the growing utilization of methane in natural gas. However, it has been a great challenge because methane has strong C-H bonds (bond energy of 413 kJ/mol) along with its perfect symmetry. It makes methane too stable to readily participate in a chemical reaction and the products are usually more reactive than methane resulting in the further oxidation. Therefore, it has been the key aspect of catalyst design to stop the oxidation at the desired products avoiding total oxidation [77,78].

Including the enzymatic systems such as methane monooxygenase (MMO) which are adept at converting methane, iron-oxygen species are known to be capable of activating the strong C-H bonds of methane [79]. In this context, Fe@Based catalysts have been widely investigated and it is obvious that these comprise a considerable portion of methane-converting materials. Fe-containing zeolite catalysts are intended to imitate the specific di-iron sites of MMO and reported to work well under mild conditions [80]. Well-dispersed

iron species over support materials act as efficient active sites in the presence of oxidants. The highly dispersed iron species over SBA-15 contribute to the selective oxidation of methane with to formaldehyde under O<sub>2</sub> atmosphere [81]. Even in the absence of oxidant methyl radicals can be derived from methane over a single iron atom embedded in silica matrix [82]. Counteranions in FePO<sub>4</sub> and Fe<sub>2</sub>(MoO<sub>4</sub>)<sub>3</sub> act as a spacer and lead to the high dispersion of iron species, which is found to be effective in the partial oxidation of methane [83,84].

Boron nitride (BN) materials have attracted an interest as an in-organic analogy of graphene due to not only the remarkable hexagonal structure, but also the noteworthy properties such as high structural, thermal stability under oxidative atmosphere and excellent thermal conductivity [85]. With wide opportunities of application, the BN materials have been used in catalysis for dispersing and stabilizing transition metal particles [86,87]. Recently, as single-atom catalyst (SAC) is considered to promising way to enhance catalytic activity, the single metal sites in the well-defined BN layers have been eagerly studied by theoretical method [88,89]. Herein, we applied semi-crystalline BN as a substrate to provide specific site for iron atoms and disperse iron species by facile thermal decomposition method. Semi-crystalline BN, which is featured by incomplete bonds and defect sites, could contribute to anchor or confine the active phase preventing the active metal species from immigration or agglomeration [90]. Through various analyses, the synthesized catalyst with low Fe loading (0.8 wt%) was found to contain single Fe sites in BN matrix whereas Fe nanoparticles were observed over

the higher loading (2.4 wt%) catalyst. The catalytic performance of the as-prepared catalysts is investigated by applying to the selective oxidation of methane. The enhanced catalytic activity over 0.8Fe@BN suggests that the atomically dispersed Fe sites have a principal role as active sites.

## **3.2 Experimental**

### **3.2.1 Preparation of catalysts**

Boron trioxide ( $B_2O_3$ , 1g) and urea ( $CO(NH_2)_2$ , 2g) were mixed in water (20 ml). The homogeneously mixed solution was recrystallized at room temperature and the white crystalline powder subsequently formed. The obtained powder was mixed with iron(III) acetylacetonate (0.0319 - 0.0978g). The mixture was placed in an alumina boat and heated in a tube furnace at 950 °C for 3 hours under  $N_2$  and  $NH_3$ . Then the tube furnace was cooled to room temperature. BN was also synthesized by using the same procedure without Fe precursor. The dried powdery samples were calcined in a stream of air at 650 °C for 2 h.

### **3.2.2 Characterization methods**

High resolution transmission electron microscopy (HR-TEM) observations were carried out on a JEOL JEM-3010 microscope operating at 300 kV. Aberration-corrected transmission electron microscopy (TEM) observations were carried out on a JEOL JEM-ARM200F operating at 200 kV. The catalyst powders were sonicated in ethanol and the dispersed on copper grids covered with a lacey carbon film. High-angle annular dark field scanning transmission microscopy (HAADF-STEM) image and corresponding elemental mapping images were acquired by means of JEOL JEM-2100F instrument equipped with an X-ray energy dispersive spectrometer.

Aberration-corrected HAADF-STEM characterization was conducted on a JEOL JEM-ARM200F with a guaranteed resolution of 0.1 nm. The Fe loadings were determined by inductively coupled plasma spectrometry (ICP-AES) on a 730ES (VARIAN) instrument. The X-ray diffraction (XRD) patterns were obtained using a Rigaku D-MAX2500-PC powder X-ray diffractometer with Cu K $\alpha$  radiation (1.5406 Å) at a scanning rate of 10.0 degree min<sup>-1</sup>. Attenuated total reflectance Fourier transform infrared measurements (FT-IR) were taken on a Nicolet 6700 in the range of 600-4000 cm<sup>-1</sup>. In the measurement 32 scans were averaged with 8 cm<sup>-1</sup> resolution. X-ray photoelectron spectroscopy (XPS) measurements were taken on AXIS SUPRA. X-ray absorption spectroscopy (XAS) was carried out in transmission mode at the 8C nano XAFS beamline of Pohang Light Source (PLS) in the 3.0 GeV storage ring, with a ring current of 70 –100 mA. X-ray absorption near edge structure (XANES) spectra were recorded for each sample at room temperature using an energy step of 0.2 eV. The obtained data were normalized by Athena software.

### **3.2.3 Measurements of catalytic performance**

The catalytic activity of the BN and Fe@BN catalysts was evaluated by selective oxidation of methane with O<sub>2</sub> as an oxidant. The catalytic reaction tests were carried out at atmospheric pressure at 600 °C. A sample of catalyst (50mg) was loaded to a quartz reactor (8 mm inner diameter) and the reactor was then placed in an electric furnace. The temperature of the catalyst bed

was monitored by a thermocouple and controlled by PID controller. Before the reaction tests, the catalyst was pre-heated to the reaction temperature under O<sub>2</sub> (2 ml/min) and He (8 ml/min) flow for 1h. The feed gases for the reaction were methane (4~10 ml/min), oxygen (2~10 ml/min), nitrogen (3 ml/min), and helium (0~8 ml/min). Nitrogen was injected as an internal standard and helium was used to balance the composition of total feed (23 ml/min). The concentrations of reactants and products in the effluent gas were analyzed by an on-line gas chromatograph (Younglin ACME 6500 model) using helium as a carrier gas.

## 3.3 Results and discussion

### 3.3.1 Structural characterization

Fe-embedded BN catalysts were prepared by the one-step pyrolytic decomposition of a mixture of boron trioxide, urea, and iron(III) acetylacetonate under  $\text{NH}_3$  atmosphere. The synthesized catalysts with Fe loading 0.8 and 2.4 wt% are denoted as 0.8Fe@BN and 2.4Fe@BN, respectively. The content of Fe in the catalysts is confirmed by inductively coupled plasma (ICP). In the representative high resolution TEM (HR-TEM) and aberration-corrected TEM images (Figure 3-1 and 3-2), it is observed that the prepared samples consist of randomly oriented BN layers. The random growth of BN layers can be seen in scanning electron microscopy (SEM) images (Figure 3-3). This highly disordered structure of as-synthesized catalysts can be described as turbostratic structure. The spacing between adjacent layers is  $\sim 0.35$  nm, which is slightly larger than the (002) plane interdistance of bulk hBN. The expanded interspace indicates the structural similarity with the turbostratic BN materials [90]. The wrinkled and branched layers of BN demonstrate the presence of defects, which could act as anchoring sites for impurities or active phase. Despite the addition of iron species as active sites, the typical iron nanoparticles are undetected over the 0.8Fe@BN catalyst. In the case of 2.4Fe@BN catalyst, however, Fe nanoparticles with a diameter of ca. 10nm can be seen. The lattice spacing of 0.21 nm in Figure 1f corresponds to the (110) crystal face of Fe nanoparticles. Also, the nanoparticles are considered to be covered by BN layers due to the

overlap between Fe nanoparticle and the amorphous area of BN (Figure 3-4). As the amount of Fe increased from 0.8 to 2.4 wt%, agglomeration of iron species may occur during the pyrolytic process and retain in the metallic form showing high resistance to oxidation because of encapsulation by BN layers. After O<sub>2</sub> treatment at 923 K, any changes in structure of 0.8Fe@BN and 2.4Fe@BN were observed (Figure 3-5).

Scanning transmission electron microscopy (STEM) and energy dispersive X-ray spectroscopy (EDS) mapping analysis were performed to obtain elemental distribution. In Figure 3-6, the element mapping of the prepared samples gave a uniform distribution of B, N, and O throughout the whole selected area without any distinguish differences among the samples. In addition, Fe element is uniformly distributed all over the BN matrix of 0.8Fe@BN as clearly shown in Figure 3b. There are no signs of distinct local intensity of Fe and it demonstrates the absence of nanoparticles. Compared with 0.8Fe@BN, several Fe-rich domains are observed over 2.4Fe@BN, though the well-dispersed Fe atoms also can be seen. It is consistent with TEM results indicating that iron nanoparticles were formed as the amount of Fe increased.

Figure 3-7 shows the X-ray diffraction (XRD) patterns of the prepared samples with different amount of iron precursor. The broad peaks at ~25° and ~43°, which are the characteristic peaks of hexagonal boron nitride, were observed and these are attributable to the (002) and (100) planes of the graphitic structure of hBN, respectively. It is found that the prepared samples show the notably low crystallinity. No clear changes in the characteristic

peak for boron nitride have been found between the prepared BN and Fe@BN samples. Consistent with TEM and STEM images above, none of Fe-related crystal phase was shown for 0.8Fe@BN whereas iron metallic peak was detected from 2.4Fe@BN. Note that no other peaks related to iron oxides are observed under the detection limit and sensibility of the XRD apparatus. As the content of Fe in BN based catalysts, however, the peaks associated with iron borate species. From the XRD pattern of 8Fe@BN catalyst, the formation of FeBO<sub>3</sub> becomes more dominant whereas the peaks for Fe<sub>3</sub>BO<sub>6</sub> are detected from 4Fe@BN (Figure 3-8).

The structural information of the prepared samples was confirmed by attenuated total reflectance Fourier transform infrared (FT-IR) spectrum (Figure 3-9). The out-of-plane B-N-B bending vibration located at 780 cm<sup>-1</sup>, while the strong in plane B-N stretching vibrations located at 1330 cm<sup>-1</sup> [91]. There is no noticeable change in the characteristic peaks of hexagonal boron nitride among the prepared samples. Consistent with the XRD result, attenuated total reflectance Fourier transform infrared (FT-IR) measurement further demonstrates that the as-synthesized catalysts are basically composed of hexagonal BN phase. Additionally, a peak at 1100 cm<sup>-1</sup>, which is assigned to B-O stretching vibrations [92], is observed for the prepared samples. It indicates that oxygen-functionalized B-terminated sites are dominant in the samples rather than N-terminated sites. After the addition of Fe and the increase of Fe content from 0.8 to 2.4 wt%, the peak for B-O stretching vibration is still detected but the intensity decreased. This change in the spectroscopic features may indicate that the O-coordinated B-terminated

sites provide anchoring site for Fe atoms. When the amount of iron in the prepared catalysts increases up to 8 wt% the intense peaks for B-O stretching and B-O-B angle bending at 1220 and 710  $\text{cm}^{-1}$ , respectively, were detected (Figure 3-10). It is considered that the B-O bondings are related to the  $\text{BO}_3$  structure of iron borate species.

The X-ray photoelectron spectroscopy (XPS) was performed to investigate the chemical composition and element states of the samples. As shown in Figure 3-11a, the dominant peak at 190.2 eV and a shoulder at 191.8 eV in B 1s spectra can be assigned to B-N and B-O bonds, respectively. The main peak at 397.8 eV in the N 1s core-level XPS spectra (Figure 3-11b) is considered as B-N bonds [19]. The typical characteristics of boron nitride are confirmed by the main peaks of the B 1s and N 1s spectra. Also, it indicates that the chemical features of those samples are very similar. In the presence of Fe atoms within BN structure, a broad shoulder peak at 530.2 eV in O 1s spectra (Figure 3-11c), which is assigned to Fe-O bonds, is observed along with B-O bonds at 532.1 eV.<sup>17</sup> In Figure 3-12, the peaks centered at 710.6 eV and 723.8 eV may be assigned to  $\text{Fe}^{3+} 2p_{3/2}$  and  $\text{Fe}^{3+} 2p_{1/2}$ , respectively [93]. From the surface concentration of B, N, O and Fe (Table 3-1), the relatively high ratio of boron to nitrogen can be found and it is in agreement with the result of FT-IR, implying the B-rich environment of the synthesized samples.

### 3.3.2 Atomically dispersed Fe species within boron nitride

X-ray absorption fine structure (XAFS) spectroscopy was used to investigate the chemical state and coordination structure of the dispersed Fe atoms. As indicated by Fe K-edge X-ray absorption near-edge structure (XANES) in Figure 3-13, the overall spectrum of Fe@BN catalysts can be separated into pre-edge and main edge. It is known that the intensity of the pre-edge peak, which appears at ~10 eV below the Fe K-absorption edge, is determined by the local coordination of iron [94]. The distinct and strong pre-edge peak of 0.8Fe@BN is usually ascribed to Fe with a tetrahedral geometry [22]. The pre-edge feature of 2.4Fe@BN is closer to the reference of Fe foil compared to that of 0.8Fe@BN, suggesting that the formation of metallic nanoparticles as the Fe content increases from 0.8 wt% to 2.4 wt%. The main edge position of Fe@BN catalysts are obviously shifted to the higher energy, compared to that of Fe foil. The absorption feature of 0.8Fe@BN is similar to that of Fe<sub>2</sub>O<sub>3</sub> and this implies that the Fe atoms in 0.8Fe@BN are mostly present in a +3 valence state. The absorption edge of 2.4Fe@BN appears at relatively lower energy compared to 0.8Fe@BN, indicating that Fe has a lower apparent oxidation state due to the presence of Fe nanoparticles shown in TEM and STEM images.

To unravel structural information on Fe atoms, extended X-ray absorption fine structure (EXAFS) has been performed, as shown in Figure 3-14. Unlike the reference, Fe foil, which has a dominant peak at 2.2 Å attributed to the Fe-Fe coordination, 0.8Fe@BN exhibited no signs for the peak

corresponding to the Fe-Fe bond. Instead, a prominent Fe-O bond with a peak at 1.5 Å is detected. This result demonstrates that Fe atoms are atomically dispersed through BN matrix of 0.8Fe@BN without Fe-Fe coordination and the isolated Fe atom is coordinated by oxygen. It is considered that a Fe site would be connected to O atoms, coordinating to the B-terminated sites of BN. In the case of 2.4Fe@BN, Fe-Fe (2.2 Å) and Fe-O (1.5 Å) bonding peaks were observed. The presence of Fe-Fe peak strongly corroborates the formation of metallic Fe nanoparticles during the pyrolytic method. However, it is found that the partially dispersed Fe atoms, shown in Figure 3-6, are coordinated by oxygen atoms.

### **3.3.3 Catalytic performance over Fe@BN catalysts**

The catalytic performances of the BN and Fe@BN catalysts for the selective oxidation of methane by oxygen are shown in Figure 3-15 and 3-16. The introduction of iron into BN significantly enhanced catalytic performance. Especially, 0.8Fe@BN catalyst exhibited the highest conversion of methane (~27 %) and selectivity (~52 %) for formaldehyde at 873 K among the samples. The methane conversion on 0.8Fe@BN is 3-fold higher than that on BN. This remarkable increase in methane conversion clearly reveals the effect of the atomically dispersed Fe sites on methane activation. This favorable CH<sub>4</sub> activation on isolated Fe<sup>3+</sup> site is consistent with what was reported previously [95,96]. With the increase of the Fe content in catalysts from 0.8 to 2.4 wt%, the conversion of methane and

selectivity of formaldehyde decreased to 22 % and 45 %, respectively. Despite the structural similarities, this difference in the catalytic performance between 0.8Fe@BN and 2.4Fe@BN can indicate that single site of Fe is more advantageous for this reaction than its nanoparticle counterpart. In consideration of the catalytic performance of 2.4Fe@BN catalyst, it contains both active Fe atoms and inactive Fe nanoparticles. These Fe@BN catalysts are superior to previously known catalysts in terms of methane conversion and space time yield (STY) of formaldehyde. In spite of the same amount of Fe, the STY of formaldehyde on 0.8Fe@BN is 8 times higher than that on 0.8wt% FeOx/SBA-15 (Figure 3-17).

In Figure 3-18, the influence of partial pressure of reactants ( $P_{\text{oxygen}}$ ,  $P_{\text{methane}}$ ) on methane consumption rate over 0.8Fe@BN catalysts was studied. The existence of oxygen as a reactant is indispensable for methane conversion. The rate of methane consumption shows less than first-order respect to the  $P_{\text{oxygen}}$  and linear correlation with  $P_{\text{methane}}$  under the given reaction conditions. Based on the Eley-Rideal mechanistic model [97-99], it appears that dissociative adsorption of oxygen is required for the methane conversion on the isolated Fe sites. The hydrogen atom abstraction from methane could occur over O-adsorbed Fe sites. Due to the absence of C2 hydrocarbons in products, it is considered that the surface  $\text{CH}_3$  species or methoxide rather than methyl radical was formed from the methane activation. As a consequence, the methyl species and hydroxyl group are converted to a methanol molecule (Figure 3-19) and it is subsequently led to HCHO, CO, and  $\text{CO}_2$  by the further oxidation. The effects of  $P_{\text{oxygen}}$  and

$P_{\text{methane}}$  on selectivity of products were also investigated (Figure 3-20 and 21). The abundance of oxygen leads to the further oxidation of HCHO to CO or CO<sub>2</sub> whereas the increasing partial pressure of CH<sub>4</sub> could inhibit the further oxidation of HCHO by competing for the surface oxygen species.

Furthermore, it is noteworthy that the Fe-free BN sample is catalytically active. From the spectroscopic results, it is considered that the B-O terminals at the edges and defects in the BN matrix (>B-O-O-B<) would provide active sites for the cleavage of C-H bond within methane molecule via hydrogen atom abstraction. This observation is similar to those that reported previously for the oxidative dehydrogenation of C<sub>2</sub>-C<sub>3</sub> alkanes over B-O(H) sites at the B-N edges. The analogous distribution of products (higher selectivity of HCHO and CO compared with that of CO<sub>2</sub>) over BN, 0.8Fe@BN, and 2.4Fe@BN suggest a similar reaction mechanism for these catalysts. The suppressed total oxidation of methane (low CO<sub>2</sub> selectivity) indicates that not only the single Fe site but B-O terminals are highly dispersed throughout BN.

**Table 3-1.** Elemental composition (atom% from XPS) of BN, 0.8Fe@BN, and 2.4Fe@BN.

Sample	Atomic concentration (%)				B/N ratio
	B	N	O	Fe	
BN	44.7	42.6	12.7	0.0	1.05
0.8Fe@BN	43.9	43.3	12.2	0.6	1.02
2.4Fe@BN	44.4	41.8	13.1	0.7	1.06

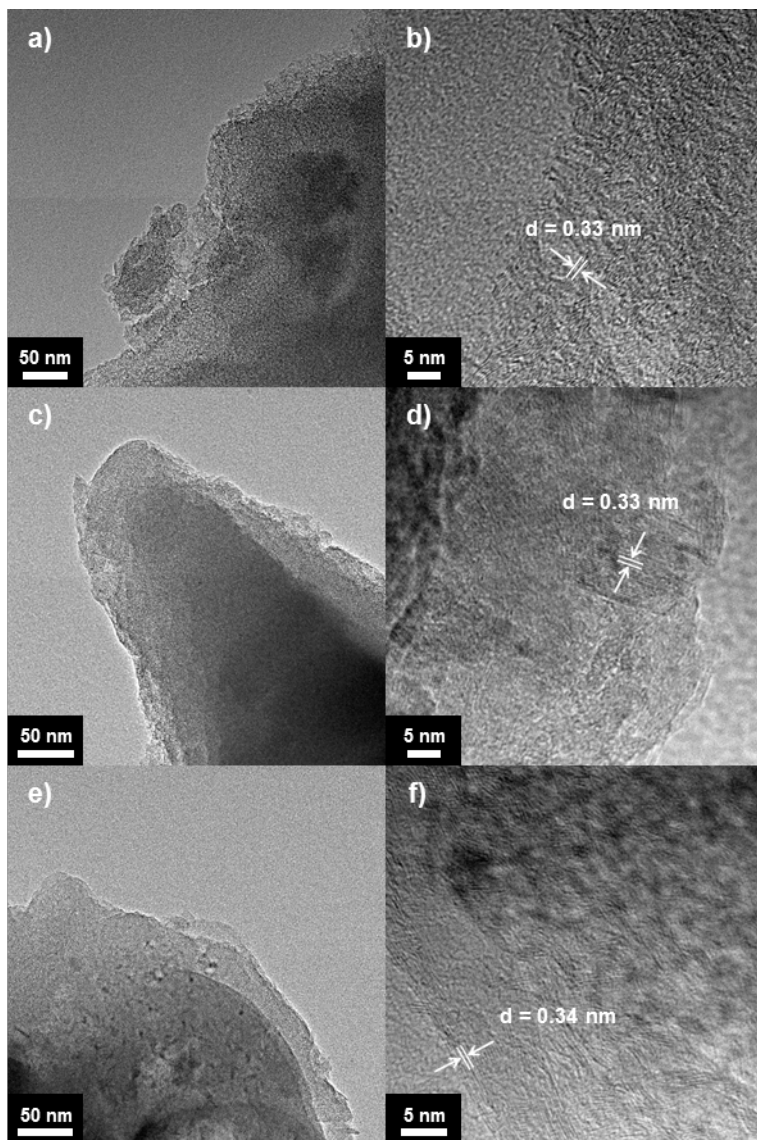


**Figure 3-1.** High-resolution TEM images of (a, b) BN, (c, d) 0.8Fe@BN, and (e, f) 2.4Fe@BN.

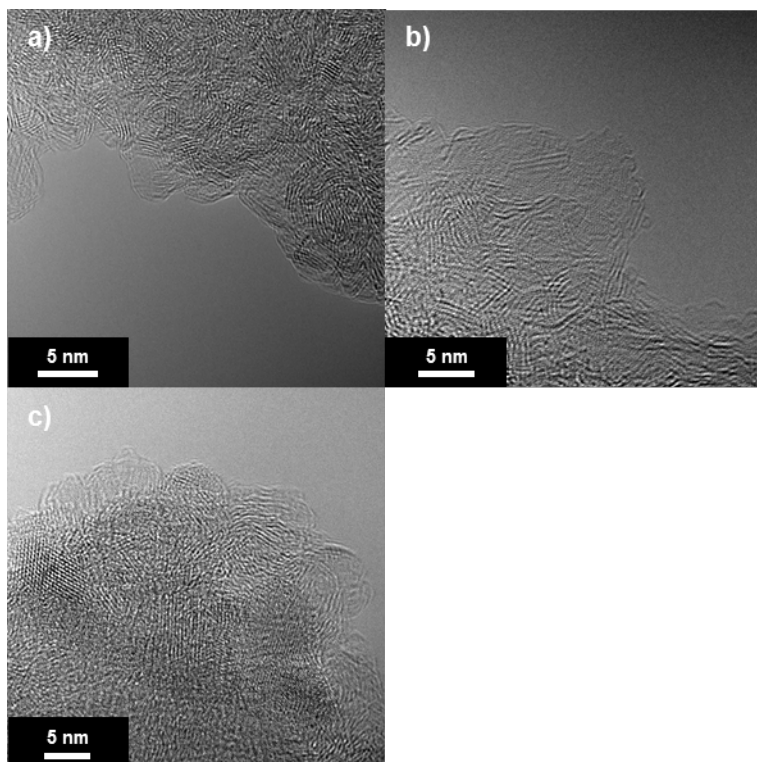


**Figure 3-2.** Aberration-corrected TEM images of (a, b) BN, (c, d) 0.8Fe@BN, and (e, f) 2.4Fe@BN.

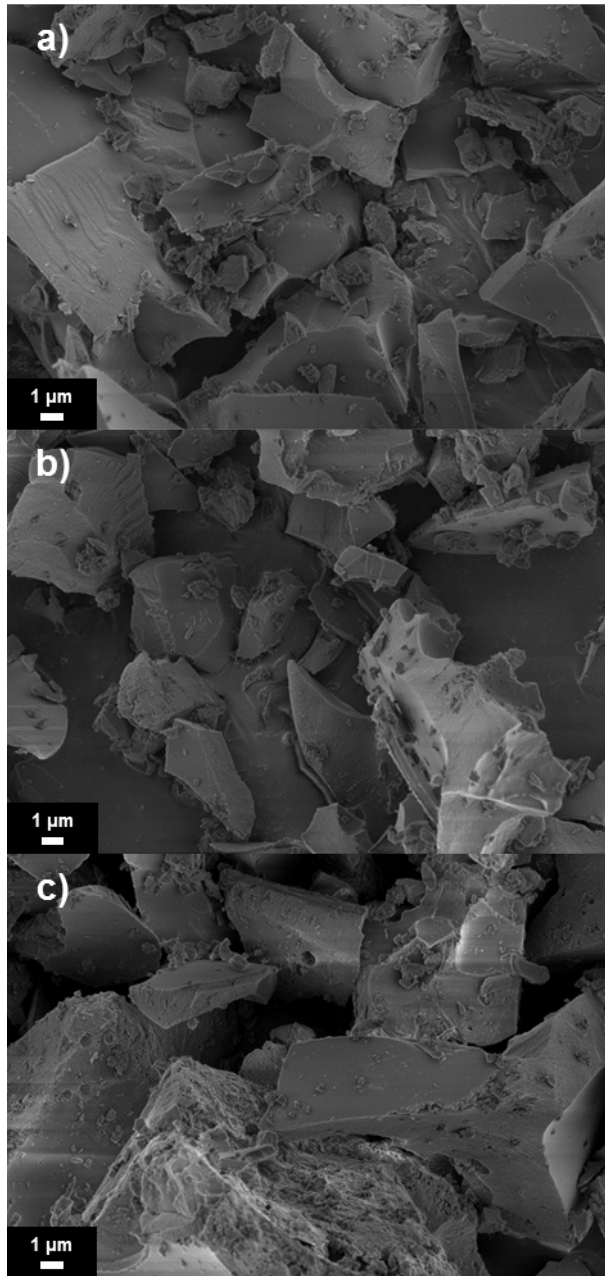


**Figure 3-3.** SEM images of (a) BN, (b) 0.8Fe@BN, and (c) 2.4Fe@BN.

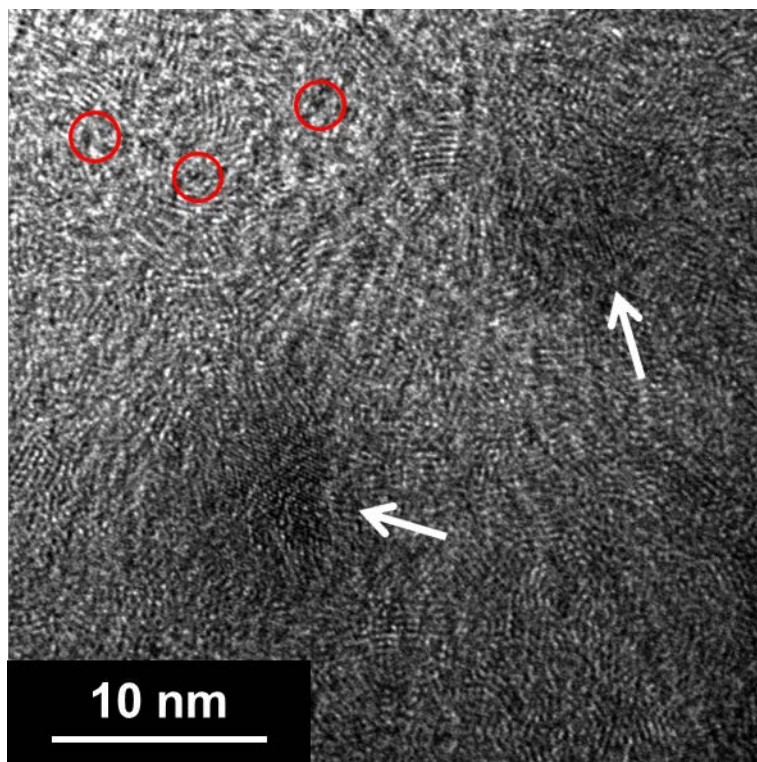


**Figure 3-4.** High-resolution TEM images of 2.4Fe@BN. The Fe nanoparticles and defects of BN are marked by white arrows and red circles, respectively.

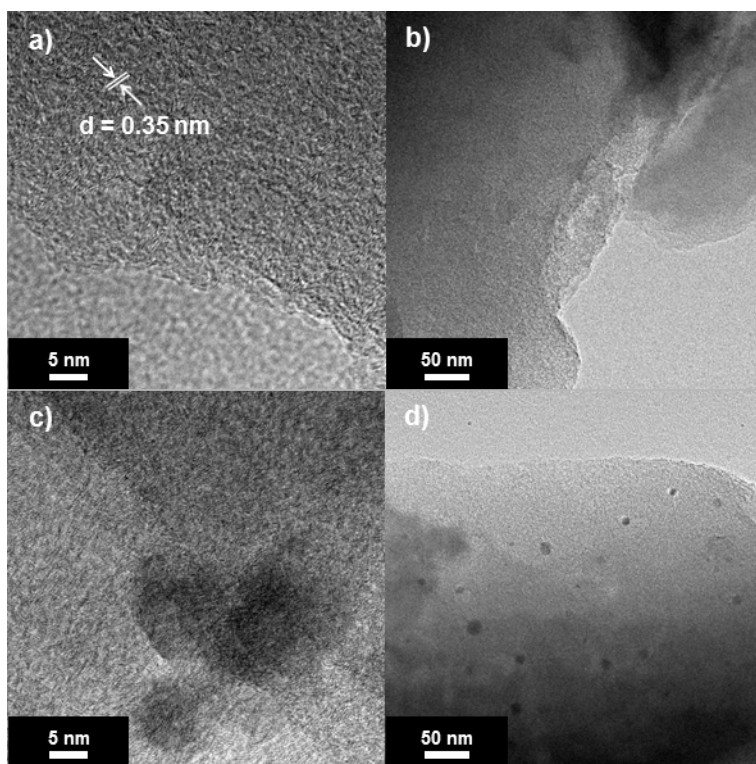


**Figure 3-5.** High-resolution TEM images of 0.8Fe@BN (a, b) and 2.4Fe@BN (c, d) after O<sub>2</sub> treatment at 650 °C for 3h.

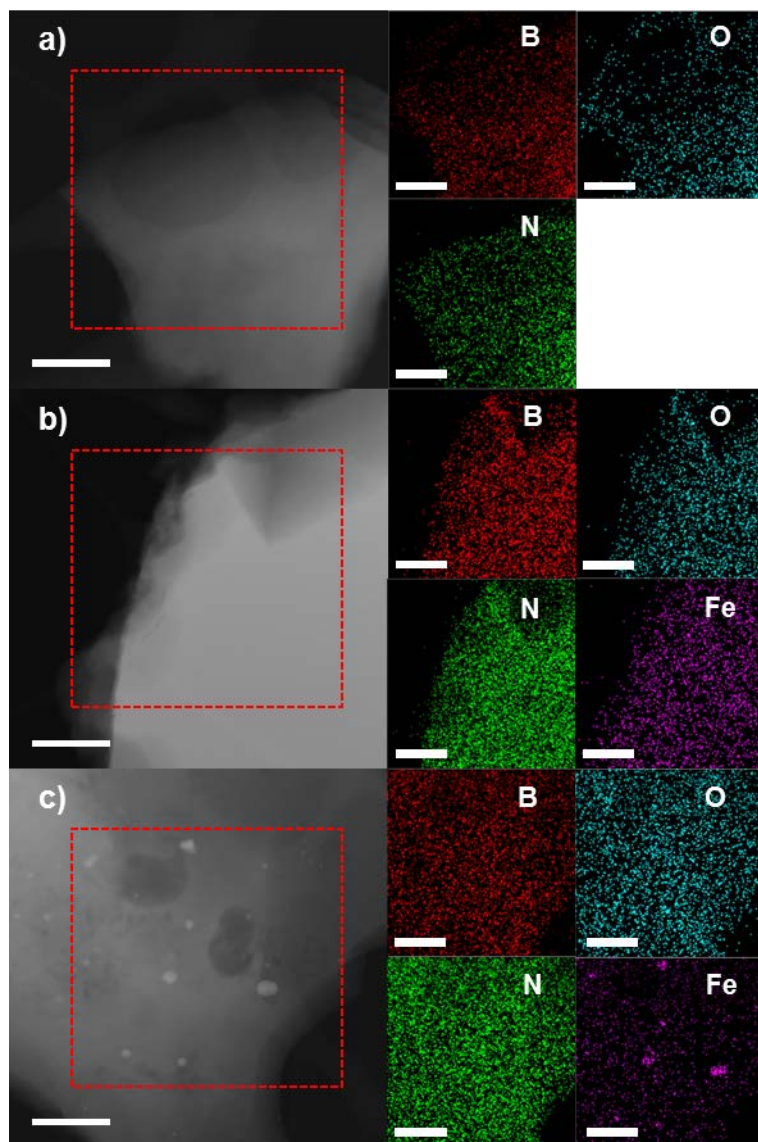


**Figure 3-6.** STEM images of a) BN, b) 0.8Fe@BN, and c) 2.4Fe@BN in the dark field mode and the elemental mapping images of B, N, O, and Fe. Scale bar, 500 nm.

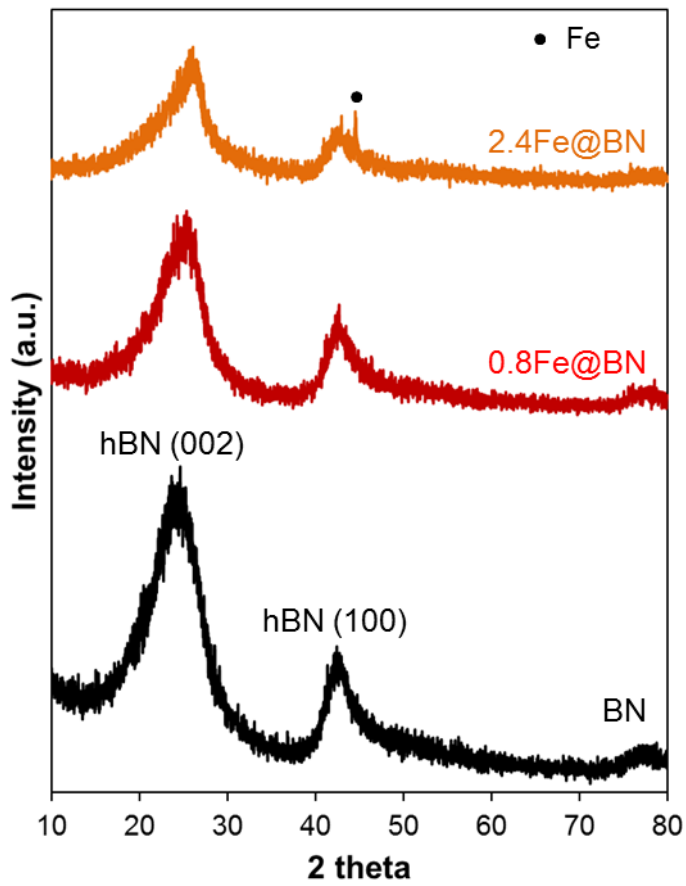


**Figure 3-7.** XRD patterns of BN, 0.8Fe@BN, and 2.4Fe@BN.

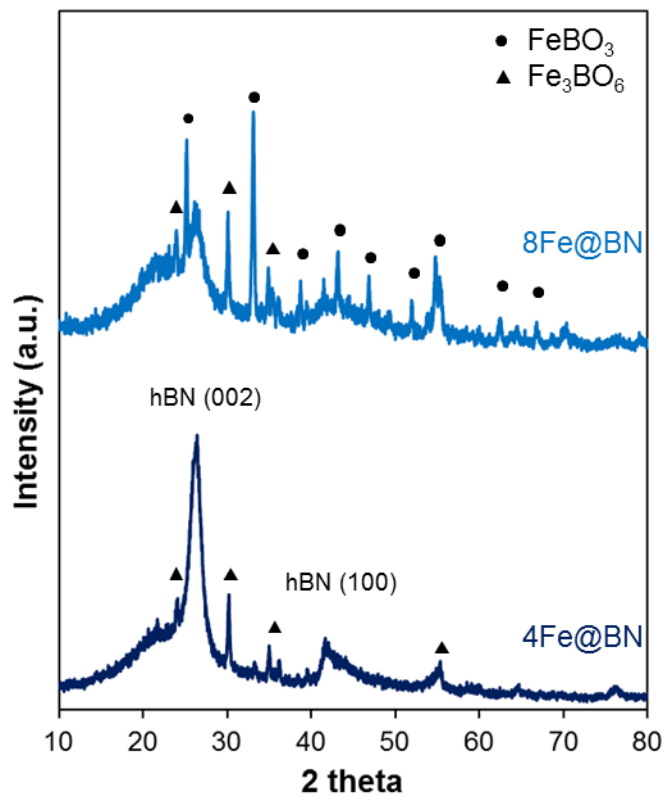


**Figure 3-8.** XRD patterns of 4Fe@BN and 8Fe@BN.

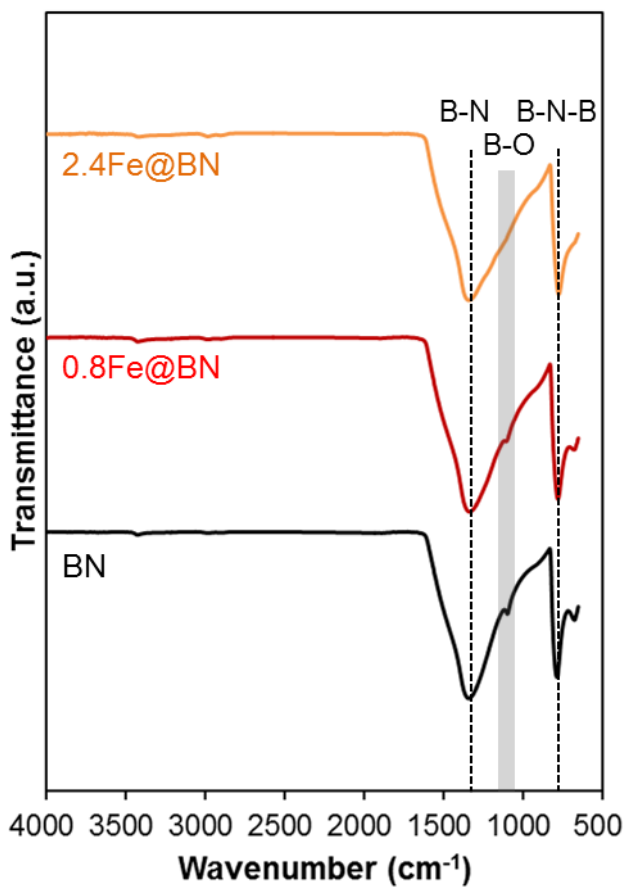


**Figure 3-9.** Attenuated total reflectance FT-IR measurement of BN, 0.8Fe@BN, and 2.4Fe@BN.

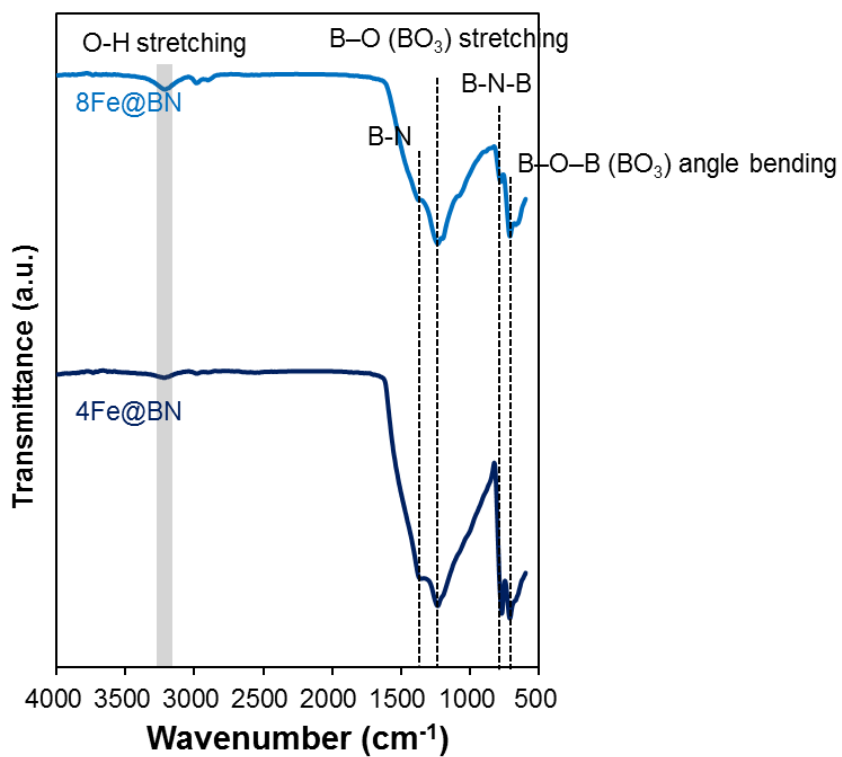


**Figure 3-10.** Attenuated total reflectance FT-IR measurement of 4Fe@BN and 8Fe@BN.

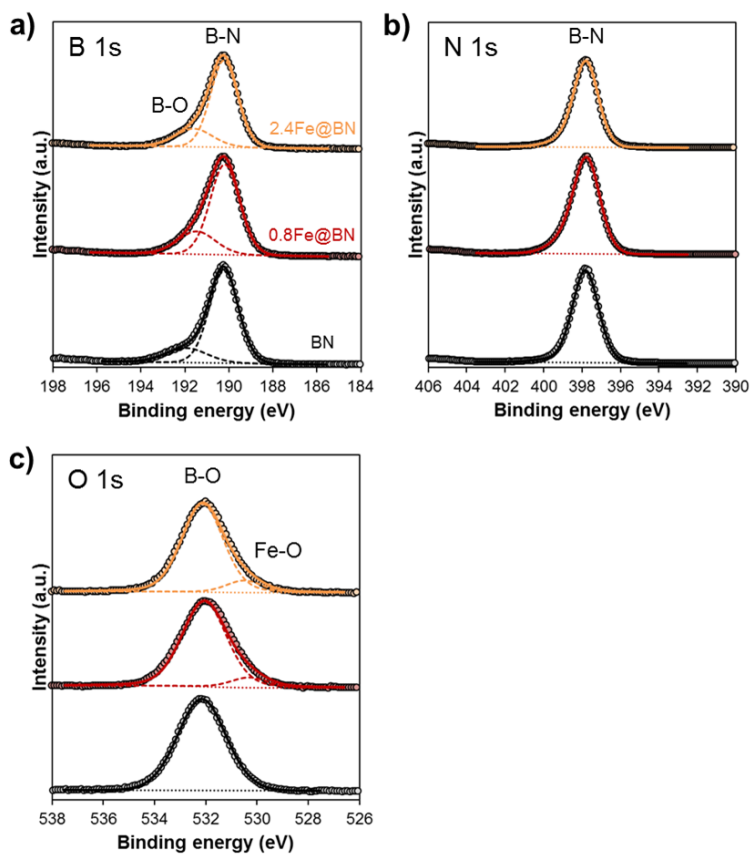


**Figure 3-11.** XPS spectra of (a) B 1s, (b) N 1s, and (c) O 1s for BN, 0.8Fe@BN, and 2.4Fe@BN.

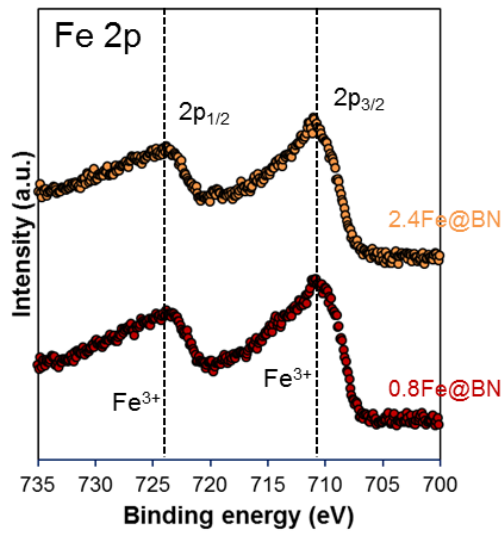


**Figure 3-12.** XPS spectra of Fe 2p for 0.8Fe@BN and 2.4Fe@BN.

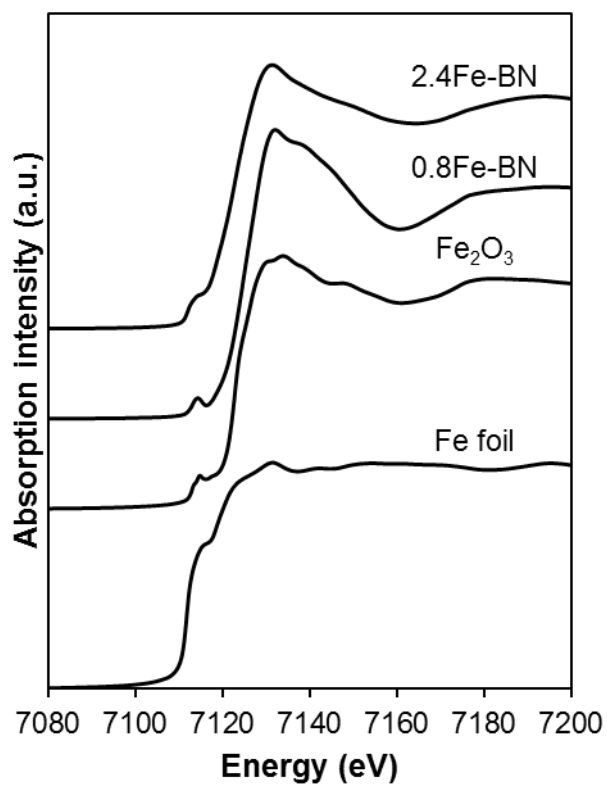


**Figure 3-13.** Fe K-edge x-ray absorption near-edge structure (XANES) spectra of Fe@BN catalysts with various Fe content in comparison to Fe foil and Fe<sub>2</sub>O<sub>3</sub>.

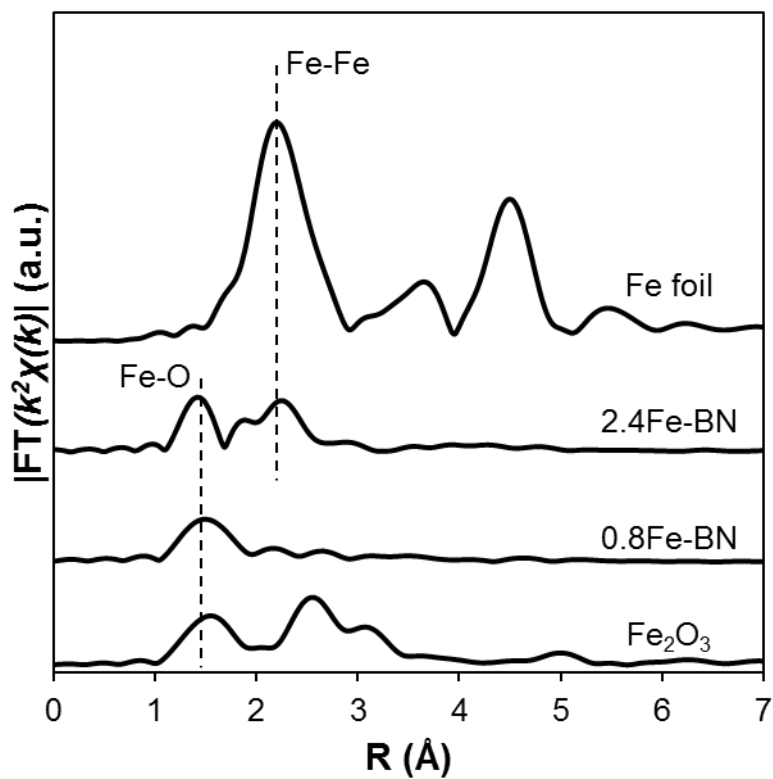


**Figure 3-14.** Fourier transform (FT) extended x-ray absorption fine structure (EXAFS) signals of Fe@BN catalysts with various Fe content in comparison to Fe foil and Fe<sub>2</sub>O<sub>3</sub>.

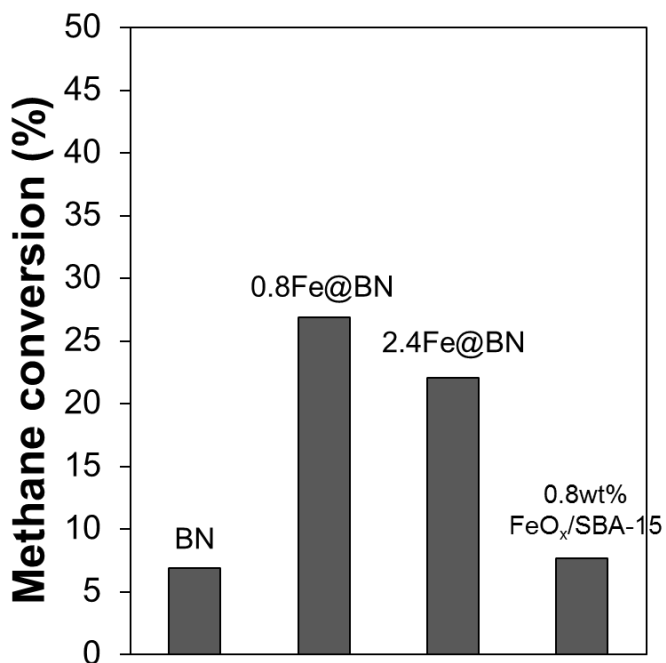


**Figure 3-15.** Methane conversion over the prepared catalysts (0.05 g) at 873 K compared with 0.8 wt% FeO<sub>x</sub>/SBA-15. FeO<sub>x</sub>/SBA-15 is a well-known catalyst for this reaction so it has been chosen for the comparison. Flow rate : CH<sub>4</sub> (10 ml/min), O<sub>2</sub> (2 ml/min), He (8 ml/min), and N<sub>2</sub> (3 ml/min).

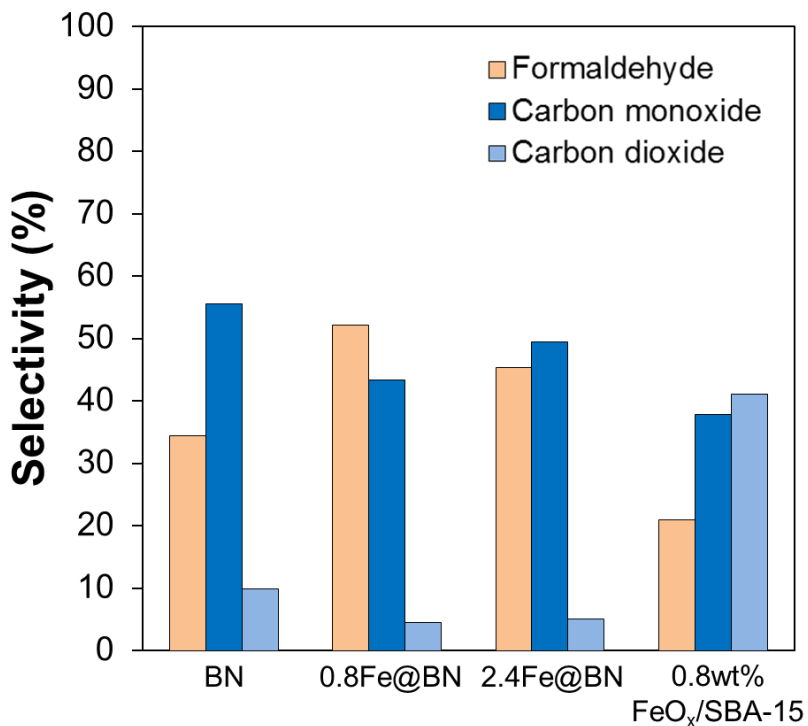


**Figure 3-16.** Product selectivity over the prepared catalysts (0.05 g) at 873 K compared with 0.8 wt% FeO<sub>x</sub>/SBA-15. FeO<sub>x</sub>/SBA-15 is a well-known catalyst for this reaction so it has been chosen for the comparison. Flow rate : CH<sub>4</sub> (10 ml/min), O<sub>2</sub> (2 ml/min), He (8 ml/min), and N<sub>2</sub> (3 ml/min).

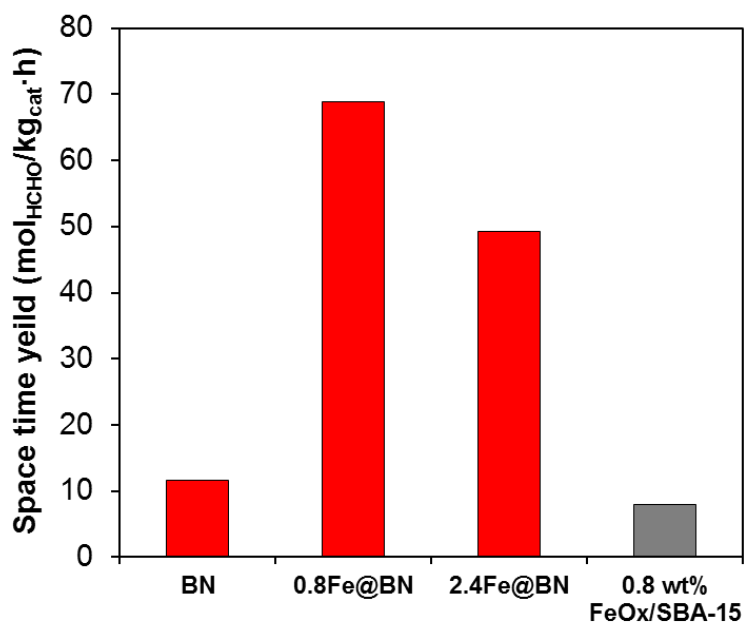


**Figure 3-17.** Space time yield (STY) of formaldehyde at 873 K over prepared samples compared with 0.8 wt% FeO<sub>x</sub>/SBA-15.

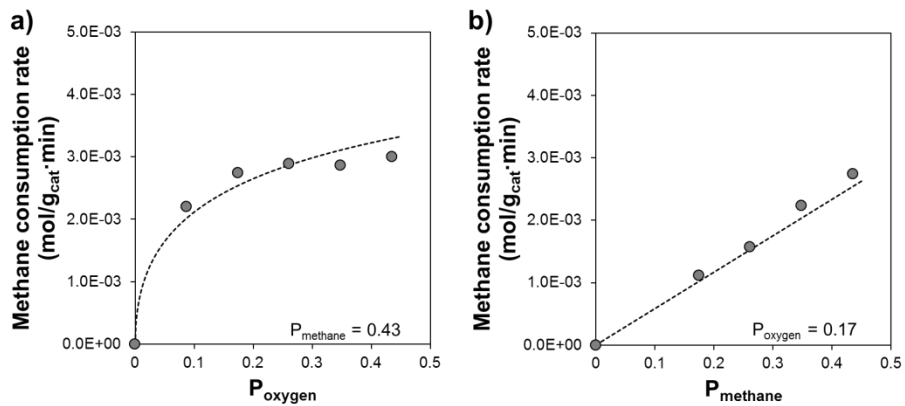


**Figure 3-18.** Dependence of methane consumption rate over 0.8Fe@BN on partial pressure of a) oxygen ( $P_{\text{oxygen}}$ ) and b) methane ( $P_{\text{methane}}$ ). He was used to balance the total pressure ( $P_{\text{total}}$  : 1atm).

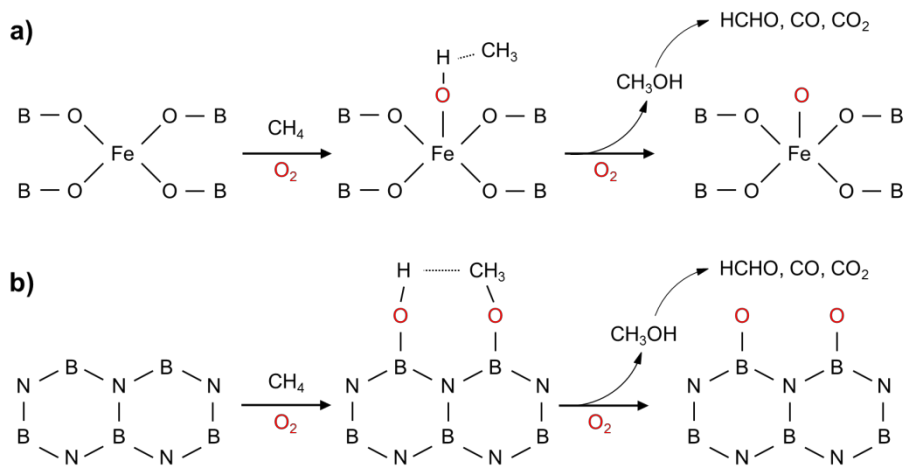


**Figure 3-19.** Schematic illustration for the selective oxidation of methane over a) single Fe site of Fe@BN catalysts and b) B-O terminals of BN material.

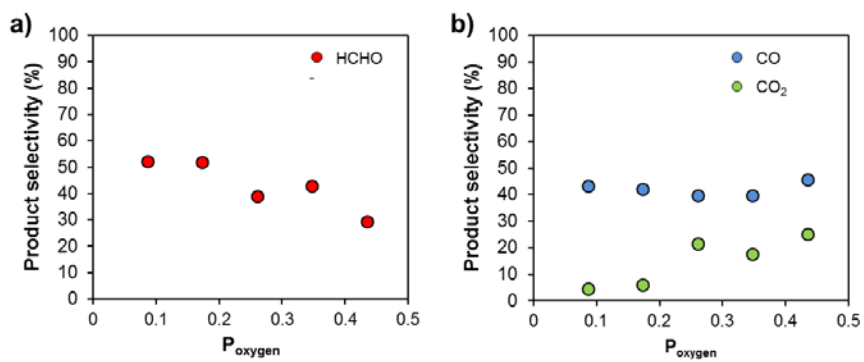


**Figure 3-20.** Effect of oxygen partial pressure ( $P_{\text{oxygen}}$ ) over 0.8Fe@BN on product selectivity.  $T = 873 \text{ K}$ ,  $P_{\text{methane}} = 0.43 \text{ atm}$ .

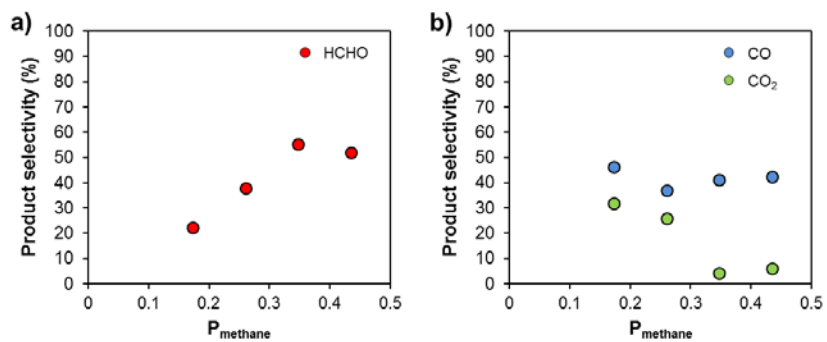


**Figure 3-21.** Effect of methane partial pressure ( $P_{\text{methane}}$ ) over Fe@BN on product selectivity.  $T = 873 \text{ K}$ ,  $P_{\text{oxygen}} = 0.17 \text{ atm}$ .

## Chapter 4. Summary and Conclusions

It has been demonstrated that atomically dispersed single Fe site within BN can be achieved by the facile pyrolytic method. Based on the well-defined BN hexagonal structure, the abundant defects and the B-terminates sites within the prepared BN materials contributed to the high dispersion of Fe atoms. The atomically dispersed Fe species were confirmed by aberration-corrected scanning transmission electron microscopy (STEM) and X-ray absorption fine structure spectroscopy (EXAFS). When the Fe-BN catalysts were applied to the selective oxidation of methane, the outstanding enhancement of catalytic activity has been exhibited. In comparison with Fe nanoparticles, the isolated Fe-O species is much more favorable to activate C-H bond in methane, form surface  $\text{CH}_3$  species or methoxide from methane rather than methyl radical. The fine-dispersion of Fe atoms contributed to suppress the further oxidation of the intermediates to  $\text{CO}_2$ . Interestingly, the prepared metal-free BN itself was catalytically active in the reaction. This work may lead to open up possibilities for the application of BN-based materials in heterogeneous catalysis.

We report a facile method to manipulate the electronic state of active metal by hetero-atom (N and B) doping technique into graphene at Co/graphene system. The similar physicochemical properties of Co/N-graphene, Co/undoped-graphene, and Co/B-graphene catalysts excluded the effects of size, phase, crystallinity, and the content of active metals on the catalytic

activity of CO hydrogenation. XPS and Raman analyses revealed that the electronic states of the supports and Co were changed according to types, concentrations, and doping structures of heteroatoms. It is considered that Co nanoparticles on N-graphene exhibited high electron density while those on B-graphene showed lower electron density compared to Co species on undoped-graphene. In reaction test, Co/N-graphene exhibited CO conversion that was 7.7-fold higher than that of Co/undoped-graphene. It is noteworthy that the catalytic activity was decreased in Co/B-graphene compared to Co/undoped-graphene. From the results, it was confirmed that catalytic activity of CO hydrogenation was controlled by tuning electronic state of Co nanoparticles toward both enhancing and reducing directions. Kinetic study revealed that variations in the catalytic activity were caused by change in the affinity of the reactants rather than change in mechanism. In the application of Pd supported graphene catalysts to 4-nitrophenol reduction reaction, the opposite trend was observed, compared to that of CO hydrogenation. The Pd/B-graphene catalyst exhibited the highest catalytic activity whereas the catalytic activity of Pd/N-graphene was retarded. The results for a 4-nitrophenol reduction reaction as well as for CO hydrogenation proved broad applications of this strategy to various reactions using transition and noble metal (Pd) catalysts.

## Bibliography

- [1] A. Balanta, C. Godard, C. Claver, *Chem. Soc. Rev.* **2011**, 40, 4973.
- [2] X. F. Yang, A. Q. Wang, B. T. Qiao, J. Li, J. Y. Liu, T. Zhang, *Acc. Chem. Res.* **2013**, 46, 1740.
- [3] B. H. Wu, Y. J. Kuang, X. H. Zhang, J. H. Chen, *Nano Today* **2011**, 6, 75.
- [4] Y. Y. Liang, Y. G. Li, H. L. Wang, J. G. Zhou, J. Wang, T. Regier, H. J. Dai, *Nat. Mater.* **2011**, 10, 780.
- [5] X. W. Xie, Y. Li, Z. Q. Liu, M. Haruta, W. J. Shen, *Nature* **2009**, 458, 746.
- [6] J. Wang, Y. Li, Y. Zhang, *Adv. Funct. Mater.* **2014**, 24, 7073.
- [7] B. F. Machado, P. Serp, *Catal. Sci. Technol.* **2012**, 2, 54-75.
- [8] M. Xu, T. Liang, M. Shi, H. Chen, *Chem. Rev.* **2013**, 113, 3766-3798
- [9] J. Deng, D. Deng, X. Bao, *Adv. Mater.* **2017**, 29, 1606967-160689.
- [10] W. Zhu, Z. Wu, G. S. Foo, X. Gao, M. Zhou, B. Liu, G. M. Veith, P. Wu, K. L. Browning, H. N. Lee, H. Li, S. Dai, H. Zhu, *Nat. Commun.* **2017**, 8, 15291-15297
- [11] F. Fuo, P. Yang, Z. Pan, X-N, Cao, Z. Xie, X. Wang, *Angew. Chem.* **2017**, 129, 8343-8347.
- [12] G. Chen, C. Xu, X. Huang, J. Ye, L. Gu, G. Li, Z. Tang, B. Wu, H. Yang, Z. Zhao, Z. Zhou, G. Fu, N. Zheng, *Nature Materials* **2016**, 15, 564-569.
- [13] Y. Bai, W. Zhang, Z. Zhang, J. Zhou, X. Wang, C. Wang, W. Huang, J. Jiang, Y. Xiong, *J. Am. Chem. Soc.* **2014**, 136(42), 14650-14653.
- [14] V. Stamenkovic, B. S. Mun, K. J. J. Mayrhofer, P. N. Ross, N. M. Markovic, J. Rossmeisl, J. Freeley, J. K. Nørskov, *Angew. Chem. Int. Ed.* **2006**, 45, 2897-2901.

- [15] V. R. Stamenkovic, B. Fowler, B. S. Mun, G. Wang, P. N. Ross, C. A. Lucas, N. M. Markovic, *Science* **2007**, 315, 493-497.
- [16] C. Chen, Y. Kang, Z. Huo, Z. Zhu, W. Huag, H. L. Xin, J. D. Snyder, D. Li, J. A. Herron, M. Mavrikakis, M. Chi, K. L. More, Y. Li, N. M. Markovic, G. A. Somorjai, P. Yang, V. R. Stamenkovic, *Science* **2014**, 343, 1339-1343.
- [17] A. A. Balandin, S. Ghosh, W. Bao, I. Calizo, DD. Teweldebrhan, F. Miao, C. N. Lau, *Nano Lett.* **2008**, 8(3), 902-907.
- [18] C. Lee, X. Wei, J. W. Kysar, J. Hone, *Science* **2008**, 321 (5887), 385-388.
- [19] S. R. Golisz, T. B. Gunnoe, W.A. Goddard, III. J. T. Groves, R. A. Periana, *Catal. Lett.* **2011**, 141, 213-221.
- [20] J. H. Lunsford, *Catal. Today* **2000**, 63, 165-174.
- [21] S. Liang, C. Hao, Y. Shi, *ChemCatChem* **2015**, 7, 2559-2567.
- [22] H. Yan, H. Cheng, H. Yi, Y. Lin, T. Yao, C. Wang, J. Li, S. Wei, J. Lu, *J. Am. Chem. Soc.* **2015**, 137, 10484-10487.
- [23] X. Yang, A. Wang, B. Qiao, J. Li, J. Liu, T. Zhang, *Acc. Chem. Res.* **2013**, 46 (8), 1740-1748.
- [24] J. K. Nørskov, T. Bligaard, J. Rossmeisl, C. H. Christensen, *Nature Chem.* **2009**, 1, 37-46.
- [25] J. C. Matsubu, S. Zhang, L. DeRita, N. S. Marinkovic, J. G. Chen, G. W. Graham, X. Pan, P. Christopher, *Nature Chem.* **2017**, 9, 120-127.
- [26] S. Cao, F. F. Tao, Y. Tang, Y. Lia, J. Yu, *Chem. Soc. Rev.* **2016**, 45, 4747-4765.
- [27] J. D. A. Pelletier, J. M. Basset, *Acc. Chem. Res.* **2016**, 49, 664-677.
- [28] J. Su, C. Xie, C. Chen, Y. Yu, G. Kennedy, G. A. Somorjai, P. Yang, *J. Am. Chem. Soc.* **2016**, 138, 11568-11574
- [29] E. Gross, J. H-C. J. Liu, F. D. Toste, G. A. Somorjai, *Nature Chem.* **2012**, 4, 947-952.

- [30] P. Tomkins, A. Mansouri, S. E. Bozbag, F. Krumeich, M. B. Park, E. M. C. Alayon, M. Ranocchiari, J. A. van Bokhoven, *Angew. Chem. Int. Ed.* **2016**, *55*, 5467-5471.
- [31] C. Li, Y. Sun, I. Djerdj, P. Voepel, C.-C. Sack, T. Weller, R. Ellinghaus, J. Sann, Y. Guo, B. M. Smarsly, H. Over, *ACS Catal.* **2017**, *7*, 6453-6463.
- [32] S. Yang, L. Peng, P. Huang, X. Wang, Y. Sun, C. Cao, W. Song, *Angew. Chem. Int. Ed.* **2016**, *55*, 4016-4020.
- [33] S. Lee, M. Choun, Y. Ye, J. Lee, Y. Mun, E. Kang, J. Hwang, Y.-H. Lee, C.-H. Shin, S.-H. Moon, S.-K. Kim, E. Lee, J. Lee, *Angew. Chem. Int. Ed.* **2015**, *54*, 9230-9234.
- [34] F. Calle-Vallejo, J. Tymoczko, V. Colic, Q. H. Vu, M. D. Pohl, K. Morgenstern, D. Loffreda, P. Sautet, W. Schuhmann, A. S. Bandarenka, *Science* **2015**, *350*, 185-189.
- [35] G. Liu, L. Zeng, Z.-J. Zhao, H. Tian, T. Wu, J. Gong, *ACS Catal.* **2016**, *6*, 2158-2162.
- [36] J. -H. Zhong, X. Jin, L. Meng, X. Wang, H.-S. Su, Z.-L. Yang, C. T. Williams, B. Ren, *Nature Nanotech.* **2017**, *12*, 132-137
- [37] D. Loffreda, C. Michel, F. Delbecq, P. Sautet, *J. Catal.* **2013**, *308*, 374-385.
- [38] Chen, G.; Xu, C.; Huang, X.; Ye, J.; Gu, L.; Li, G.; Tang, Z.; Wu, B.; Yang, H.; Zhao, Z.; Zhou, Z.; Fu, G.; Zheng, N. *Nature Mat.* **2016**, *15*, 564-571.
- [39] W. Zhu, Z. Wu, G. H. Foo, X. Gao, M. Zhou, B. Liu, G. M. Veith, P. Wu, K. L. Browning, H. N. Lee, H. Li, S. Dai, H. Zhu, *Nature Commun.* **2017**, *8*, 15291.
- [40] X. Chen, H. Jiang, B. Hou, W. Gong, Y. Liu, Y. Cui, *J. Am. Chem. Soc.* **2017**, *139*, 13476-13482.

- [41] S. Xie, S.-I. Choi, N. Lu, L. T. Roling, J. A. Herron, L. Zhang, J. Park, J. Wang, M. J. Kim, Z. Xie, M. Mavrikakis, Y. Xia, *Nano Lett.* **2014**, *14*, 3570-3576.
- [42] H. Zhang, L. Lu, K. Kawashima, M. Okumura, M. Haruta, N. Toshima, *Adv. Mater.* **2015**, *27*, 1383-1388.
- [43] S. Chen, L. Luo, Z. Jiang, W. Huang, *ACS Catal.* **2015**, *5*, 1653-1662.
- [44] S. Zhang, X. Zhang, G. Jiang, H. Zhu, S. Guo, D. Su, G. Lu, S. Sun, , *J. Am. Chem. Soc.* **2014**, *136*, 7734-7739.
- [45] M. McEntee, A. Stevanovic, W. Tang, M. Neurock, Jr. J. T. Yates, *J. Am. Chem. Soc.* **2015**, *137*, 1972-1982.
- [46] J. Xiao, X. Pan, S. Guo, P. Ren, X. Bao, *J. Am. Chem. Soc.* **2015**, *137*, 477-482.
- [47] W. Zhang, L. Wang, H. Liu, Y. Hao, H. Li, M. U. Khan, J. Zeng, *Nano Lett.* **2017**, *17*, 788-793.
- [48] J. V. Lauritsen, J. Kibsgaard, S. Helveg, H. Topsøe, B. S. Clausen, E. Lægsgaard, F. Besenbacher, *Nature Nanotech.* **2007**, *2*, 53-58.
- [49] H. Wang, C. Wang, H. Yan, H. Yi, J. Lu, *J. Catal.* **2015**, *324*, 59-68.
- [50] S. Sun, G. Zhang, N. Gauquelin, N. Chen, J. Zhou, S. Yang, W. Chen, X. Meng, D. Geng, M. N. Banis, R. Li, S. Ye, S. Knights, G. A. Botton, T.-K. Sham, X. Sun, *Sci. Rep.* **2016**, *3*, 1775.
- [51] Y. Wu, D. Wang, X. Chen, G. Zhou, R. Yu, Y. Li, *J. Am. Chem. Soc.* **2013**, *135*, 12220-12223.
- [52] H. Liu, Y. Liu, D. Zhu, *J. Mater. Chem.* **2011**, *21*, 3335-3345.
- [53] A. Kaniyoor, T. T. Baby, T. Arockiadoss, N. Rajalakshmi, S. Ramaprabhu, *J. Phys. Chem. C* **2011**, *115*, 17660-17669.
- [54] G. L. Bezemer, J. H. Bitter, H. P. C. E. Kuipers, H. Oosterbeek, J. E. Holewijn, X. Xu, F. Kapteijn, A. J. van Dillen, K. P. de Jong *J. Am. Chem. Soc.* **2006**, *128*, 3956-3964.

- [55] J. P. den Breejen, P. B. Radstake, G. L. Bezemer, J. H. Bitter, V. Frøseth, A. Holmen, K. P. de Jong, *J. Am. Chem. Soc.* **2009**, *131*, 7197-7203.
- [56] J. Lu, L. Yang, B. Xu, Q. Wu, D. Zhang, S. Yuan, Y. Zhai, X. Wang, Y. Fan, Z. Hu, *ACS Catal.* **2014**, *4*, 613-621.
- [57] R. N. Grass, W. J. Stark, *J. Mater. Chem.* **2006**, *16*, 1825-1830.
- [58] T. Sharifi, G. Hu, X. Jia, T. Wågberg, *ACS Nano* **2012**, *6*, 8904-8912.
- [59] H. Tao, Y. Gao, N. Talreja, F. Guo, J. Texter, C. Yan, Z. Sun, *J. Mater. Chem. A* **2017**, *5*, 7257-7284.
- [60] T. Schiros, D. Nordlund, L. Pálová, D. Prezzi, L. Zhao, K. S. Kim, U. Wurstbauer, C. Gutiérrez, D. Delongchamp, C. Jaye, D. Fischer, H. Ogasawara, L. G. M. Pettersson, D. R. Reichman, P. Kim, M. S. Hybertsen, A. N. Pasupathy, *Nano Lett.* **2012**, *12*, 4025-4031.
- [61] S. Jaliliab, R. Vaziri, *Mol. Phys.* **2011**, *109*, 687-694.
- [62] M. Sahoo, K.P. Sreena, B.P. Vinayan, S. Ramaprabhu, *Mat. Res. Bull.* **2014**, *61*, 383-390.
- [63] P. Lazar, R. Zbořil, M. Pumera, M. Otyepka, *Phys. Chem. Chem. Phys.* **2014**, *16*, 14231-14235.
- [64] Agnoli, S.; Favarob, M. *J. Mater. Chem. A* **2016**, *4*, 5002-5025.
- [65] H. Zhang, X. Pan, J. J. Liu, W. Qian, F. Wei, Y. Huang, X. Bao, *ChemSusChem* **2011**, *4*, 975-980.
- [66] S.-J. Liang, L. K. Ang, *Phys. Rev. Appl.* **2015**, *3*, 014002.
- [67] J.-H. Kim, J. H. Hwang, J. Suh, S. Tongay, S. Kwon, C. C. Hwang, J. Wu, J. Y. Park, *Appl. Phys. Lett.* **2013**, *103*, 171604.
- [68] *CRC Handbook of Chemistry and Physics* version **2008**, p.12-114.
- [69] P. Rani, V. K. Jindal, *RSC Adv.* **2013**, *3*, 802-812.
- [70] J. Yang, Y. Qi, J. Zhu, Y.-A. Zhu, D. Chen, A. Holmen, *J. Catal.* **2013**, *308*, 37-49.

- [71] M. Ojeda, R. Nabar, A. U. Nilekar, A. Ishikawa, M. Mavrikakis, E. Iglesia, *J. Catal.* **2010**, *272*, 287-297.
- [72] B. Yoon, H. Häkkinen, U. Landman, A. S. Wörz, J.-M. Antonietti, S. Abbet, K. Judai, U. Heiz, *Science* **2005**, *307*, 403-407.
- [73] Z. D. Pozun, S. E. Rodenbusch, E. Keller, K. Tran, W. Tang, K. J. Stevenson, G. Henkelman, *J. Phys. Chem. C* **2013**, *117*, 7598-7604.
- [74] L. Liu, R. Chen, W. Liu, J. Wub, D. Gaob, *J. Hazard. Mat.* **2016**, *320*, 96-104.
- [75] A. Caballero, P. J. Perez, *Chem. Soc. Rev.* **2013**, *42*, 8809.
- [76] C. Hammond, S. Conrad, I. Hermans, *ChemSusChem* **2012**, *5*, 1668.
- [77] P. Tang, Q. Zhu, Z. Wu, D. Ma, *Energy Environ. Sci.* **2014**, *7*, 2580.
- [78] Z. Guo, B. Liu, Q. Zhang, W. Deng, Y. Wang, Y. Yang, *Chem. Soc. Rev.* **2014**, *43*, 3480.
- [79] C. E. Tinberg, S. J. Lippard, *Acc. Chem. Res.* **2011**, *44*, 280.
- [80] B. Michalkiewicz, *Appl. Catal., A* **2004**, *277*, 147.
- [81] Q. Zhang, Y. Li, D. An, Y. Wang, *Appl. Catal., A* **2009**, *356*, 103.
- [82] McCormick, R. L.; Alptekin, G. O. *Catalysis Today* **2000**, *55*, 269.
- [83] K. Otsuka, Y. Wang, I. Yamanaka, A. Morikawa, *J. Chem. Soc. Faraday Trans.*, **1993**, *89*, 4225.
- [84] X. Guo, G. Fang, G. Li, H. Ma, H. Fan, L. Yu, C. Ma, X. Wu, D. Deng, M. Wei, D. Tan, R. Si, S. Zhang, J. Li, *Science* **2014**, *344*, 616.
- [85] R. T. Paine, C. K. Narula, *Chem. Rev.* **1990**, *90*, 73.
- [86] C. Huang, W. Ye, Q. Liu, X. Qiu, *ACS Appl. Mater. Interfaces* **2014**, *6*, 14469.
- [87] P. Wu, W. Zhu, A. Wei, B. Dai, Y. Chao, C. Li, H. Li, S. Dai, *Chem. Eur. J.* **2015**, *21*, 15421.
- [88] K. Mao, L. Li, W. Zhang, Y. Pei, X. C. Zeng, X. Wu, J. Yang, *Sci. Rep.* **2014**, *4*, 5441.
- [89] M. Gao, A. Lyalin, T. Taketsugu, *J. Phys. Chem. C* **2012**, *116*, 9054.

- [90] S. Alkoy, C. Toy, T. Gönül, A. Tekin, *J. Eur. Ceram. Soc.* **1997**, 17, 1415.
- [91] D. Lee, B. Lee, K. H. Park, H. J. Ryu, S. Jeon, S. H. Hong, *Nano Lett.* **2015**, 15, 1238.
- [92] T. Sainsbury, A. Satti, P. May, Z. Wang, I. McGovern, Y. K. Gun'ko, J. Coleman, *J. Am. Chem. Soc.* **2012**, 134, 1.
- [93] R. A. Silva-Molina, E. Muñoz-Sandoval, R. Gámez-Corrales, R. A. Guirado-López, *J. Phys. Chem. C* **2015**, 119, 25576.
- [94] Q. Fu, Y. Meng, Z. Fang, Q. Hu, L. Xu, W. Gao, X. Huang, Q. Xue, Y-P. Sun, F. Lu, *ACS Appl. Mater. Interfaces* **2017**, 9, 2469.
- [95] J. A. Sigrist, M. W. Gaultois, A. P. Grosvenor, *J. Phys. Chem. A* **2011**, 115, 1908.
- [96] Q. Zhang, Q. Guo, X. Wang, T. Shishido, Y. Wang, *J. Catal.* **2006**, 239, 105.
- [97] T. E. Westre, P. Kennepohl, J. G. DeWitt, B. Hedman, K. O. Hodgson, E. I. Solomon, *J. Am. Chem. Soc.* **1997**, 119, 6297.
- [98] K. Otsuka, Y. Wang, *Appl. Catal., A* **2001**, 222, 145.
- [99] F. Arena, A. Parmaliana, *Acc. Chem. Res.* **2003**, 36, 867.

## 국 문 초 록

화학 공정의 생산성 증가와 비용 절감을 위한 노력의 일환으로 효율적인 촉매의 개발에 대한 노력은 꾸준히 유지되어 왔다. 금속 나노입자 기반의 촉매에서 담체와 금속 나노입자 간의 상관관계에 의한 촉매 성능 변화에 대한 연구들이 보고됨에 따라서 담체 물질에 대한 연구도 증가 하고 있다. 그 중에서도 그래핀과 질화붕소는 특징적인 육각구조와 넓은 표면적, 높은 안정성 등을 바탕으로 불균일계 촉매 반응에 대해 많이 응용되고 있다. 본 논문에서는 이원자 물질의 첨가를 통해 그래핀과 질화붕소의 특성 변화를 유도해 촉매로서의 성능을 증가시키거나 고분산된 활성점을 형성하고자 하였다.

그래핀의 주성분인 탄소와 비교해 원자내에 전자가 하나 많거나 하나 적은 질소 혹은 붕소를 그래핀에 도핑함으로써 그래핀의 전자적인 상태를 조절하고자 하였다. 열처리 온도에 따라서 그래핀에 도핑된 질소와 붕소의 농도와 구조가 변화하는 것을 확인하였다. 이러한 변화로 인해 이원자가 도핑된 그래핀에 담지되어 있는 코발트나 팔라듐의 전자상태가 조절되는 것을 관찰할 수 있었다. 이렇게 담지된 금속(코발트와 팔라듐)의 전자 상태의 변화는 각각 일산화탄소의 수소화 반응과 4-니트로페놀 환원 반응에서의 촉매 활성에 영향을 미쳤다는 것을 반응

실험을 통해 확인하였다.

메탄의 선택적 산화 반응을 통한 메탄올 및 포름알데하이드 생성 반응은 안정한 구조의 메탄과 반응성이 좋은 생성물(메탄올, 포름알데하이드)로 인해서 많은 제한점이 존재하고 있다. 그래핀과 유사한 구조를 가지고 있는 질화붕소를 담체로 사용한 단원자 촉매를 제조하고자 하였다. 이를 통해 탄소와 수소의 결합을 분해할 수 있는 활성점의 수를 최대화하고 중간 생성물의 연속적인 산화 반응을 방지하기 위해 활성점이 고분산될 수 있도록 하고자 하였다. 질소와 붕소 전구체의 열분해 반응을 통해 제조한 질화붕소는 기본적으로 육각구조를 나타내고 있지만 불규칙하고 많은 결합을 가지고 있어 금속(철) 입자를 고정하기에 유리하였다. 따라서 불규칙한 구조를 가지고 있는 질화붕소를 담체로 응용하여 철은 고분산된 단원자 상태로 유지될 수 있었다. 메탄의 선택적 산화반응에 대해서 제조된 철 단원자 촉매는 철 나노입자가 담지된 촉매와 비교해 높은 메탄의 전환율과 포름알데하이드의 선택도를 나타내었다.

주요어: 불균일계 촉매작용, 단원자 촉매, 메탄, 선택적 산화반응, 도핑, 전자상태, 그래핀, 수소화반응

학 번: 2014-31078

# List of publications

## International Publications

### International Academic Published Papers (First Author)

1. **H. Park**, Y. S. Yun, T. Y. Kim, K. R. Lee, J. Baek, and J. Yi, "Kinetics of the dehydration of glycerol over acid catalysts with an investigation of deactivation mechanism by coke", *Applied Catalysis B: Environmental*, **2015**, 176, 1-10.
2. Y. Choi\*, **H. Park\***, Y. S. Yun, and J. Yi, "Effects of Pore Structures and Acid Properties on the Catalytic Dehydration of Glycerol", *ChemSusChem*, **2015**, 8(6), 974-979.

(\* Youngbo Choi and Hongseok Park contributed equally to this work.)

### International Academic Published Papers (Co-author)

1. D. Yun\*, D. S. Park\*, K. R. Lee, Y. S. Yun, T. Y. Kim, **H. Park**, H. Lee and J. Yi "A New Energy-Saving Catalytic System: CO<sub>2</sub> Activation via Metal/Carbon Catalyst", *ChemSusChem*, **2017**, 10, 3671-3678
2. D. Yun, Y. S. Yun, T. Y. Kim, **H. Park**, J. M. Lee, J. W. Han, and J. Yi, "Mechanistic Study of Glycerol Dehydration on Brønsted Acidic Amorphous Aluminosilicate", *Journal of Catalysis*, **2016**, 341, 33-43.
3. Y. S. Yun, K. R. Lee, **H. Park**, T. Y. Kim, D. Yun, J. W. Han, and J. Yi, "Rational Design of a Bi-functional Catalyst for the Oxydehydration of Glycerol: A Combined Theoretical and Experimental Study", *ACS Catalysis*, **2015**, 5, 82-94.
4. Y. Choi\*, Y. S. Yun\*, **H. Park**, D. S. Park, D. Yun, and J. Yi, "A facile approach for preparation of tunable acid nano-catalyst with hierarchically mesoporous

structure", *Chemical Communications*, **2014**, 57(50), 7652-7655.

## Patents

1. 이종협, 박대성, 윤다님, 윤양식, **박홍석**, “금속이 분산된 열린 기공구조를 가지는 탄소 촉매 및 이를 이용한 소르비톨의 생산방법”, 대한민국특허 **등록** 10-1535123 (2015.07.02)
2. 이종협, 최영보, **박홍석**, 윤양식, “3차원의 열린 기공 구조를 갖는 산성 산화물 나노 입자, 그 제조방법 및 상기 나노 입자를 이용하여 글리세롤로부터 아크롤레인 또는 아크릴산을 제조하는 방법”, 대한민국특허 **등록** 10-1504673 (2015.03.16)
3. 이종협, 최영보, 윤양식, **박홍석**, 윤다님, “3차원의 열린 기공 구조를 갖는 알루미늄실리케이트 구형 나노 입자, 그 제조방법 및 상기 나노 입자를 이용하여 글리세롤로부터 아크릴산을 제조하는 방법”, 대한민국특허 **등록** 10-1337301 (2013.11.29)

## International Conferences (First author)

1. **H. Park**, Y. S. Yun, D. Yun, T. Y. Kim, K. R. Lee, J. Baek, M. Lee, and J. Yi, “An investigation of deactivation mechanism by coke via kinetics study of the glycerol dehydration over acid catalysts”, 16th International Congress on Catalysis, CNCC, Beijing, China, July. 3-July. 8 (2016)
2. **H. Park**, Y. Choi, Y. S. Yun, and J. Yi, “Oxy-dehydration of biomass-derived glycerol over acidic nanosphere catalysts with hierarchically mesoporous structures”, The 14th Japan-Korea Symposium on Catalysis, WINC Aichi, Nagoya, Japan, July 1-3 (2013)
3. **H. Park**, Y. S. Yun, K. R. Lee, and J. Yi, “Dehydration of Glycerol over Hierarchically Mesoporous Acid Catalysis”, The Korean Society of Clean Technology 2014 Fall Meeting, K hotel, Gyeongju, Korea, Sep. 24-26 (2014)

4. H. Park, Y. Choi, Y. S. Yun, and J. Yi, "Oxy-dehydration of biomass-derived glycerol over acidic nanosphere catalysts with hierarchically mesoporous structures", The 14th Japan-Korea Symposium on Catalysis, WINC Aichi, Nagoya, Japan, July 1-3 (2013)
5. **H. Park**, Y. Choi, Y. S. Yun, and J. Yi, "(Oxy)dehydration of glycerol over wrinkled and 3D porous acid nanosphere", The 6th WCU International Symposium on Chemical Convergence for Energy and Environment, Sheraton Hotel, Incheon, Korea, June 17-18 (2013)
- 6.

### International Conferences (Co-author)

1. Y. Kim, T. Y. Kim, **H. Park**, C. K. Song, H. Lee, and J. Yi, "The Effect of Oxidants on Methanol Production for Direct Oxidation of Methane over Cu-MOR", The 16th Korea-Japan Symposium on Catalysis, Kaderu 27, Sapporo, Japan, May. 15-May. 17 (2017)
2. Y. S. Yun, K. R. Lee, **H. Park**, T. Y. Kim, D. Yun, J. W. Han, and J. Yi, "Bi-Functional Mo-V-W-O Catalysts for the One-Step Production of Acrylic Acid from Glycerol and Validation Via First Principle Calculations", 24th North American Catalysis Society Meeting, David L. Lawrence Convention Center, Pittsburgh, Pennsylvania, USA, June. 14-June. 19 (2015)
3. Y. S. Yun, T. Y. Kim, D. Yun, **H. Park**, J. M. Lee, J. W. Han, and J. Yi, "Mechanistic insight of hydrogenolysis of glycerol over Cu-based catalysts via ab initio calculations", The 15th Korea-Japan Symposium on Catalysis, BEXCO and Haundae Centum Hotel, Busan, Korea, May. 26-May. 28 (2015)
4. Y. S. Yun, K. R. Lee, **H. Park**, Y.-J. Seo, W. G. Kim, J. W. Han, and J. Yi, "Tungsten oxide promoted molybdenum vanadium mixed oxide catalysts for oxydehydration of glycerol", The Korean Society of Clean Technology 2014 Fall Meeting, K hotel, Gyeongju, Korea, Sep. 24-26 (2014)

5. K. R. Lee, Y. S. Yun, **H. Park**, Y.-J. Seo, W. G. Kim, and J. Yi, "Development of Scale-up Method of Glycerol Conversion to Bench Scale Reaction", The Korean Society of Clean Technology 2014 Fall Meeting, K hotel, Gyeongju, Korea, Sep. 24-26 (2014)
6. D. S. Park, D. Yun, Y. S. Yun, **H. Park**, T. Y. Kim, J. Baek, and J. Yi, "Direct conversion of lignocellulose to sugar alcohols over Pt supported on a new 3D mesoporous carbon", 247th American Chemical Society National Meeting & Exposition, Dallas, Texas, USA, Mar. 16-20 (2014)
7. Y. S. Yun, Y. Choi, **H. Park**, D. Yun, and J. Yi, "Three dimensionally open porous acid catalysts with adjustable acidic properties", The 14th Japan-Korea Symposium on Catalysis, WINC Aichi, Nagoya, Japan, July 1-3 (2013)
8. K. R. Lee, Y. S. Yun, **H. Park**, Y.-J. Seo, W. G. Kim, and J. Yi, "Development of Scale-up Method of Glycerol Conversion to Bench Scale Reaction", The Korean Society of Clean Technology 2014 Fall Meeting, K hotel, Gyeongju, Korea, Sep. 24-26 (2014)
9. **H. Park**, Y. S. Yun, K. R. Lee, and J. Yi, "Dehydration of Glycerol over Hierarchically Mesoporous Acid Catalysis", The Korean Society of Clean Technology 2014 Fall Meeting, K hotel, Gyeongju, Korea, Sep. 24-26 (2014)
10. D. S. Park, D. Yun, Y. S. Yun, **H. Park**, T. Y. Kim, J. Baek, and J. Yi, "Direct conversion of lignocellulose to sugar alcohols over Pt supported on a new 3D mesoporous carbon", 247th American Chemical Society National Meeting & Exposition, Dallas, Texas, USA, Mar. 16-20 (2014)
11. Y. S. Yun, Y. Choi, **H. Park**, D. Yun, D. S. Park, and J. Yi, "Preparation of 3D Open-Porous Acidic Heterogeneous Catalysts for the Chemical Production", 2013 MRS Fall Meeting Program & Exhibit, Boston, Massachusetts, USA, Dec. 1-6 (2013)

12. S. Park, E. H. Kim, M. Eo, H. D. Song, H. Park, J. Roh, J. Yoon, Y. Kim, and J. Yi, "Transport behavior of silver nanoparticles in soil", 243rd ACS National Meeting & Exposition, San Diego, California, USA, March 25-29 (2012)

## Domestic Conferences

1. 윤양식, 윤다님, 김태용, 이경록, **박홍석**, 송찬경, 김윤화, 이민재, 성종백, 이종협, 한정우, "구리금속 및 구리-크롬 복합 산화물 촉매에서의 글리세롤 수소화분해 반응 메커니즘 연구", 한국화학공학회 2017년도 봄 총회 및 학술대회, 제주 ICC, 4. 26-28 (2017)
2. 윤다님, 윤양식, 김태용, **박홍석**, 한정우, 이종협, "비정질 알루미늄실리케이트 촉매의 브룬스테드 산 점에서 글리세롤 탈수반응 메커니즘 연구", 한국화학공학회 2016년도 가을 총회 및 학술대회, 대전컨벤션센터, 10. 19-21 (2016)
3. 송찬경, 백자연, 유성주, 김태용, 윤다님, **박홍석**, 이경록, 이종협, "TiO<sub>2</sub> 상과 구조적 효과에 의한 가시광선 영역에서 Au/TiO<sub>2</sub>의 광촉매 활성 분석", 한국화학공학회 2016년도 봄 총회 및 학술대회, 부산 BEXCO, 4. 27-29 (2016)
4. **박홍석**, 윤양식, 김길표, 이민재, 송현돈, 서영중, 김왕규, 이종원, 이종협, "산 촉매에서의 글리세롤 탈수반응에 대한 반응속도론적 연구", 한국화학공학회 2014년도 가을 총회 및 학술대회, 대전컨벤션센터, 10. 23-24 (2014)
5. 윤양식, 이경록, **박홍석**, 김태용, 윤다님, 서영중, 김왕규, 이종원, 한정우, 이종협, "글리세롤의 산화탈수반응을 위한 이원기능촉매 개발 및 적용", 한국화학공학회 2014년도 가을 총회 및 학술대회, 대전컨벤션센터, 10. 23-24 (2014)
6. **박홍석**, 윤양식, 이경록, 이종협, "글리세롤의 산화탈수반응을 통한 아크릴산 생산 기술 개발", 2014년 한국청정기술학회 춘계 학술발표회, 여수경도리조트, 3. 27-28 (2014)
7. 윤양식, **박홍석**, 이경록, 이종협, "글리세롤로부터 프로판다이올 및 바이오 고분자 생산기술 개발", 2014년 한국청정기술학회 춘계 학술발표회, 여수

경도리조트, 3. 27-28 (2014)

8. 윤양식, **박홍석**, 윤다님, 박대성, 김태용, 백자연, 이경록, 이종협, “계층구조를 갖는 나노크기의 고체산촉매 제조 및 응용”, 2014년 한국청정기술학회 춘계 학술발표회, 여수경도리조트, 3. 27-28 (2014)
9. 백자연, 송현돈, 김태용, 박대성, 윤다님, 윤양식, **박홍석**, 이종협, “금 나노입자의 암모니아 보란을 이용한 4-니트로페놀 환원 반응에서의 실시간 전자이동 관찰”, 2013년 한국청정기술학회 추계 학술발표회, 제주 한화리조트, 9. 25-27 (2013)
10. **박홍석**, 최영보, 윤양식, 이종협, “3차원 계층 구조의 다공성 나노 산 촉매를 이용한 글리세롤의 산화탈수반응”, 한국화학공학회 2013년 봄 총회 및 학술대회, 광주 김대중컨벤션센터, 4. 24-26 (2013)
11. 윤양식, 최영보, **박홍석**, 이종협, “글리세롤을 아크릴산으로 직접 전환하기 위한 이원기능촉매의 제조 및 분석”, 한국화학공학회 2013년 봄 총회 및 학술대회, 광주 김대중컨벤션센터, 4. 24-26 (2013)
12. 윤양식, 최영보, 윤다님, **박홍석**, 이종협, “글리세롤의 산화탈수반응을 위한 다공성 산성 나노촉매의 제조 및 분석”, 한국화학공학회 봄 총회 및 학술대회, 제주국제컨벤션센터, 4.25-27 (2012)